LUT UNIVERSITY

LUT School of Energy Systems

LUT Mechanical Engineering

Niko Riikonen

CHARACTERIZATION OF PART DEFORMATIONS IN POWDER BED FUSION OF STAINLESS STEEL

Examiner: Docent Heidi Piili

TIIVISTELMÄ

Niko Riikonen

Jauhepetisulatuksella ruostumattomasta teräksestä valmistettujen kappaleiden muodonmuutosten karakterisointi

Tämän tutkimuksen tavoitteena oli tutkia, miksi ja millaisia muodonmuutoksia syntyy metallisiin kappaleisiin, jotka ovat valmistettu jauhepetisulatuksella. Kirjalliseen osaan etsittiin ja kerättiin tietoa aikaisemmista tutkimuksista, joiden aiheena on metalliosien muodonmuutokset jauhepetisulatuksessa. Kokeellisessa osassa tutkittiin metallikappaleiden muodonmuutoksia erilaisissa geometrioissa, kun koekappaleet valmistettiin jauhepetisulatuksella ruostumattomasta teräksestä.

Kirjallisuusosan päätuloksia oli, että kappaleen suuri lämpötila kasvattaa sula-altaan kokoa, hidastaa jäähtymistä sekä madaltaa kappaleen myötölujuuden arvoa, mikä altistaa kappaleen muodonmuutoksille. Jauhepetisulatuksessa metallikappaleiden muodonmuutokset määräytyvät lämpögradienttien mukaan. Vetojäännösjännitys muodostuu kappaleen pintaan, kun taas puristusjäännösjännitys kappaleen sisäosaan. Tyypillistä on, että mahdollisen muodonmuutoksen tapahtuessa kappaleen reunat nousevat rakennusalustasta korkeiden jäännösjännitysten vaikutuksesta. Suurimmat jäännösjännityspiikit muodostuvat rakennussuunnassa, koska suurimmat lämpögradientit vaikuttavat rakennussuunnassa ennemmin kuin vaakatasossa. Myös suurimmat muodonmuutokset havaitaan rakennussuunnassa.

Kokeellisessa osassa valmistettiin erilaisia geometrioita erilaisissa asennoissa ja huomattiin, että muodonmuutoksia syntyi vaakatasossa sekä 45° kulmassa valmistettuihin koekappaleisiin. Nämä muodonmuutokset noudattavat muotoa, jossa kappaleen reunat nousevat ylös rakennusalustasta johtuen korkeista jäännösjännityksistä. Pystyasennossa sekä kyljellään rakennettujen koekappaleiden kohdalla ei havaittu muodonmuutoksia, kappaleen geometriasta riippumatta. Kappaleen orientaatiolla on siis merkittävä vaikutus muodonmuutosten syntyyn jauhepetisulatuksessa. Jokainen erilainen geometria pystyttiin valmistamaan ilman muodonmuutosta, orientaatiota muuttamalla.

ABSTRACT

LUT University
LUT School of Energy Systems
LUT Mechanical Engineering

Niko Riikonen

Characterization of part deformations in powder bed fusion of stainless steel

Master's thesis

2019

78 pages, 56 figures and 10 tables

Examiner: Docent Heidi Piili

Keywords: Additive manufacturing, powder bed fusion, stainless steel, heat, defect, deformation, thermal stress, residual stress.

Aim of this thesis was to study why deformations occur in metal parts made by laser powder bed fusion and what is the deformation shape. This thesis was done by conducting a literature review by searching and collecting data from studies relating to the topic of metal part deformations in laser powder bed fusion and performing an experimental part in which the deformations of stainless steel parts were examined by manufacturing different geometries by laser powder bed fusion and capturing their deformations by macroscope.

As results from literature part, higher temperature of the part increases melt pool size, lowers cooling rate and lowers yield strength of the material, exposing the part for deformations. Deformation of metal parts made by laser powder bed fusion obeys the temperature gradient mechanism that aims to lift the edges of parts from the building platform due to residual stresses. Tensile residual stresses are generated on the surface of the part whereas compressive stresses locate inside the part. Higher temperature gradients exist in the building direction rather than in horizontal plane which results in the highest residual stress peaks in the building direction. Also the largest deformations are observed in the building direction rather than horizontally.

Different geometries were built in different orientations in the experimental part and it was observed that deformations occurred in test samples built horizontally and in 45° angle when positioned flat on the building platform. The deformation shapes obeyed the temperature gradient mechanism and as a result, the edges of parts bent upwards from the building platform. No deformations were observed in test samples built vertically or horizontally on their side, regardless of the geometry of the part. Orientation of the part plays an important role in generation of deformations in laser powder bed fusion. Each test sample geometry could be manufactured without deformation, by adjusting the orientation of the part.

ACKNOWLEDGEMENTS

TABLE OF CONTENTS

LIST OF SYMBOLS AND ABBREVIATIONS

σ_{comp} Compressive Stress

σ_{tens} Tensile Stress

AM   Additive Manufacturing

ASTM   American Society for Testing and Materials

CAD   Computer Aided Design

HAZ   Heat Affected Zone

ISO   International Organization for Standardization

L-PBF   Laser Powder Bed Fusion

SS   Stainless Steel

TGM   Temperature Gradient Mechanism

1   INTRODUCTION

Additive manufacturing (AM) gives such freedom for manufacturing unique and complex shapes that is not possible to achieve by other manufacturing technologies (Wohlers et al. 2018, p. 17-18). Especially the AM technologies that utilize metal material are gaining interest in the manufacturing industry due to the possibility of production of high performance end-use parts (Wohlers et al. 2018, p. 149, 157-158, 173-174). However, there are also some challenges with metal AM and defect related challenges are studied in this thesis (Wohlers et al. 2018, p. 185).

1.1 Research problem

The most popular metal AM technology, laser powder bed fusion (L-PBF), is capable of producing strong, high quality and high performance parts with complex shapes (Wohlers et al. 2018, p. 161, 173-174). However, L-PBF has its limitations due to the cyclic heat delivery that is inherent in the process. Cyclic heat delivery leads to subsequent expansion and contraction of the material which creates stresses in the part during the build. These stresses can rise higher than the yield strength of the material which causes deformations in the parts either during the build or while removing the parts from the building platform when the residual stresses are released. (Masoomi et al. 2017, p. 73-74; Simson et al. 2017, p. 184-185; Yang et al. 2017, p. 599.) When the heat is continuously applied to the part during the build, the part is exposed for accumulation of heat and increase of part temperature (Yang & Wang 2008, p. 1066). The heat conducts from the top layer to the building platform through the part. Therefore, geometry of the part has an effect on the heat transfer and accumulation of heat in the part. (Mukherjee et al. 2018b, p. 373.) These heat related challenges form the research problem of this thesis.

1.2 Aim of research and research questions

Motivation for this thesis was to search the challenges that relate to manufacturing metal parts by L-PBF. As L-PBF induces cyclic heat delivery to the material, it causes residual stresses in parts and exposes them for deformations (Masoomi et al. 2017, p. 73-74; Yang et al. 2017, p. 599). The deformations can be so large that the parts cannot be used in their function. Aim of this thesis is to study why deformations occur in parts made by L-PBF and

what is the deformation shape. The deformations relate to errors in the outer shape of the part. This thesis will seek answers for the following research questions:

- Why deformations occur?
- What kind of deformation shape can be expected?
- How to prevent deformations?

This thesis has industrial relevance as interest in metal AM has been strongly growing among manufacturing industry and L-PBF is proceeding towards serial production of high quality end-use parts (Wohlers et al. 2018, p. 149, 157-158, 173-174). It is important to recognize both the possibilities and challenges of L-PBF in order to adopt the technology into use.

1.3 Research methods and framing

Research methods of this thesis consist of literature review and experimental part. Literature review is a theoretical frame to the thermal phenomena and their effect on the formation of deformations in L-PBF of metal. Mainly relatively recent articles (published since 2014) relating to the topic of metal part deformations in L-PBF are used as references in this thesis. Based on the information collected in the literature review, deformation behavior of metal parts was examined in the experimental part by designing different shapes with computer aided design (CAD) software, manufacturing the test samples by L-PBF and capturing their deformation with a macroscope, aiming to clarify the reasons for the deformations.

This thesis focuses in L-PBF of metal material and the experimental part is executed with stainless steel (SS) 316L. The deformations discussed through the thesis relate to dimensional errors in the outer shape of the part and do not include internal defects such as porosity or lack of fusion in the part.

2   LITERATURE REVIEW

L-PBF is an AM process that includes subsequent rapid melting and solidification of the powder and nearby regions of already solidified material in a multi-layer, multi-hatch builds (Mukherjee et al. 2018b, p. 369). A schematic of a multi-layer, multi-hatch build is represented in figure 1.
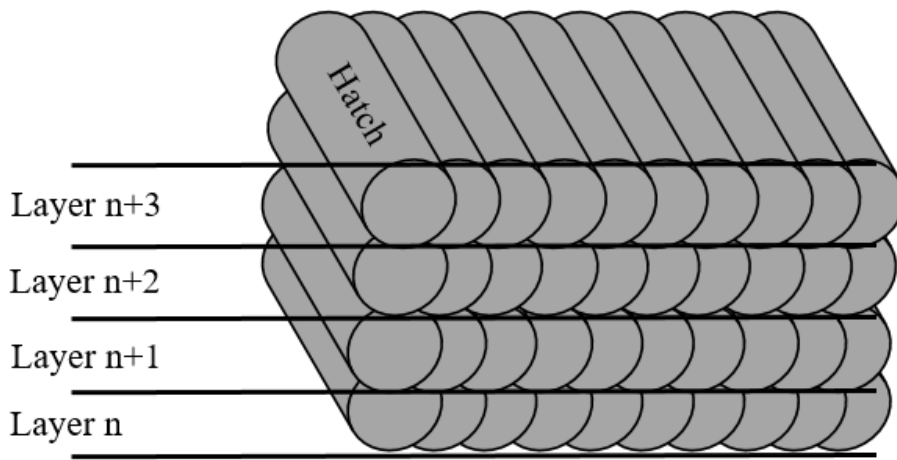

Figure 1. Schematic of a multi-hatch, multi-layer build (4 layers with 10 hatches each).

Cyclic thermal load applied to the part during the build creates residual stresses due to subsequent thermal expansions and contractions of the material, which makes the part being built, exposed to deformations in either manufacturing stage or post-processing stages (Masoomi et al. 2017, p. 73-74; Yang et al. 2017, p. 599). Thermal phenomena of the process must be recognized to be able to better understand the vulnerability of metal parts for defects and deformations in L-PBF. One key phenomenon that affects the formation of deformations in L-PBF of metal is heat transfer, as it affects the temperature field, local cooling, build shape and size of the melt pool and the reach of fusion region in the part. (Bertoli et al. 2017, p. 385-386; Ilin et al. 2014, p. 398-399; Mukherjee et al. 2018b, p. 369.) This will be discussed in this chapter.

2.1 Effect of heat

Mukherjee et al. (2018b) studied the thermal phenomena of L-PBF with SS 316. They created a model to estimate different thermal phenomena that SS 316 will encounter during

L-PBF. The model was included with parameters represented in table 1 (Mukherjee et al. 2018b, p. 370).

Table 1. Parameters used in modeling of the thermal phenomena of SS 316 in L-PBF (Mukherjee et al. 2018b, p. 370).

Laser power	60 W
Focal point diameter	100 µm
Layer thickness	25-35 µm
Scanning strategy	Unidirectional along positive x-axis
Material	SS 316

The model to predict the effect of laser scanning speed on the melt pool geometry for four different scanning speeds in a single track experiment was created by Mukherjee et al. (2018b, p. 371). Results are represented in figure 2.
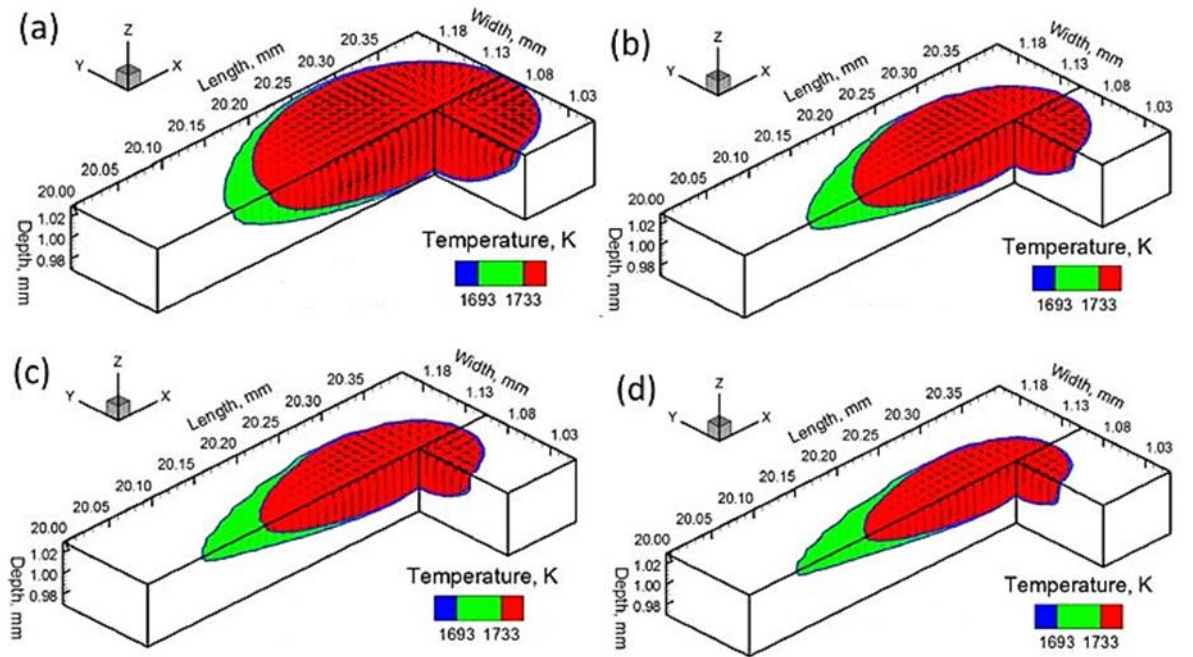

Figure 2. Single track melt pool geometries with temperature contours with scanning speed of (a) 250 mm/s (b) 500 mm/s (c) 750 mm/s and (d) 1000 mm/s and laser power of 60 W. Other parameters are same as in table 1. (Mukherjee et al. 2018b, p. 371.)

In figure 2, red region indicates the melt pool in which the material is in molten state. Green region indicates the material mushy zone in which the material solidifies. White region behind the mushy zone indicates already solidified material. Temperature in the mushy zone (green) is between solidus (1693 K) and liquidus (1733 K) temperature, specific for SS 316. Laser beam travel is in direction of positive x-axis. (Mukherjee et al. 2018b, p. 370-371.) As it can be seen in figure 2, higher scanning speed results in smaller melt pool by volume because of lower heat input to the material per unit length. However, melt pool is longer with higher scanning speed but does not penetrate in the material and extend as wide as with lower scanning speed. (Bertoli et al. 2017, p. 393; Ilin et al. 2014, p. 394; Li & Gu 2014, p. 106; Mukherjee et al. 2018b, p. 370-371.) Figure 3 represents the thermal cycle of the previous single track experiment in which temperatures are measured in the track mid-length, on the top surface. The temperature peak is observed at a time when the laser beam scans right on top of the measuring point. (Mukherjee et al. 2018b, p. 371-372.)
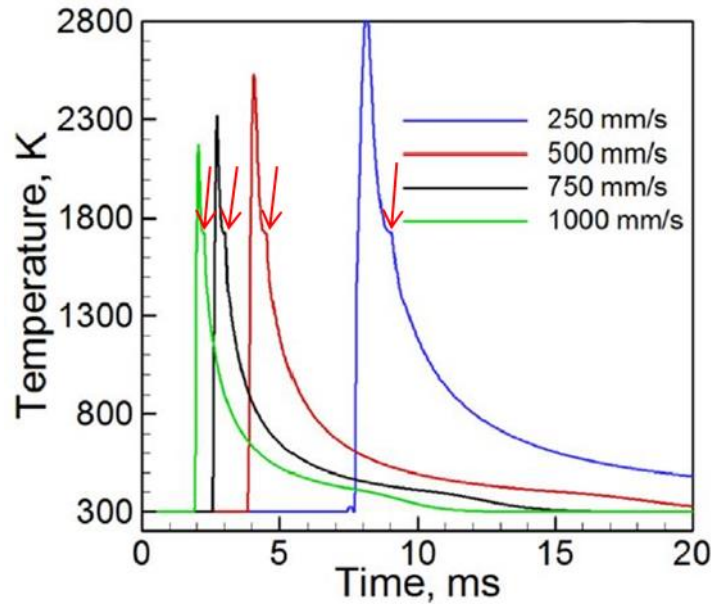

Figure 3. Thermal cycles of four different scanning speeds, measured in track mid-length, on top surface. Laser power of 60 W, other parameters are same as in table 1. (Modified from Mukherjee et al. 2018b, p. 372.)

As figure 3 illustrates, the lowest scanning speed results in highest peak temperature because of the highest heat input to the material. Higher scanning speed rapidly swipes through the scanning path, resulting in lower heat delivery to the material. (Li & Gu 2014, p. 104; Mukherjee et al. 2018b, p. 371-372.) Therefore, higher heat input leads to both higher

temperatures in the build and larger melt pool as it can be stated based on figures 2 and 3. In addition, higher heat input leads to slower cooling of the scanned area which can be obtained in figure 3 by comparing the width of the temperature peaks. Highest scanning speed has the narrowest temperature peak which indicates the fastest cooling. During cooling, a small shoulder (highlighted by red arrow in figure 3) can be noticed in the temperature peaks between the solidus and liquidus temperatures, which is the stage of material being solidified, the mushy zone. The shoulder in the temperature peaks is at the same temperature for all the scanning speeds examined because solidus and liquidus temperatures are material related values. (Li et al. 2017, p. 161; Mukherjee et al. 2018b, p. 371-372.)

Thermal cycle for also a multi-hatch scan was examined by Mukherjee et al. (2018b, p. 372). Unidirectional scanning strategy in which laser beam travel is only along the positive x-axis (20 mm scanning length) during the whole build, was used. Top surface, in the track mid-length of the first hatch, was chosen as measuring point for the thermal cycles for 10 hatches in a single layer. (Mukherjee et al. 2018b, p. 370-372.) Measuring point is illustrated in figure 4.
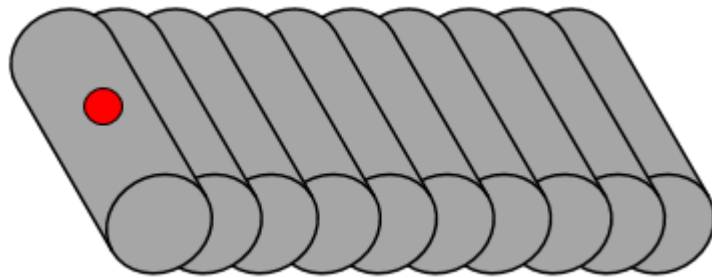

Figure 4. Measuring point (red dot) of the thermal cycles in a single layer, 10 hatch build (Mukherjee et al. 2018b, p. 372).

The model describes the planar effect of heat during the build of one layer. The thermal cycles are represented in figure 5 (Mukherjee et al. 2018b, p. 372).
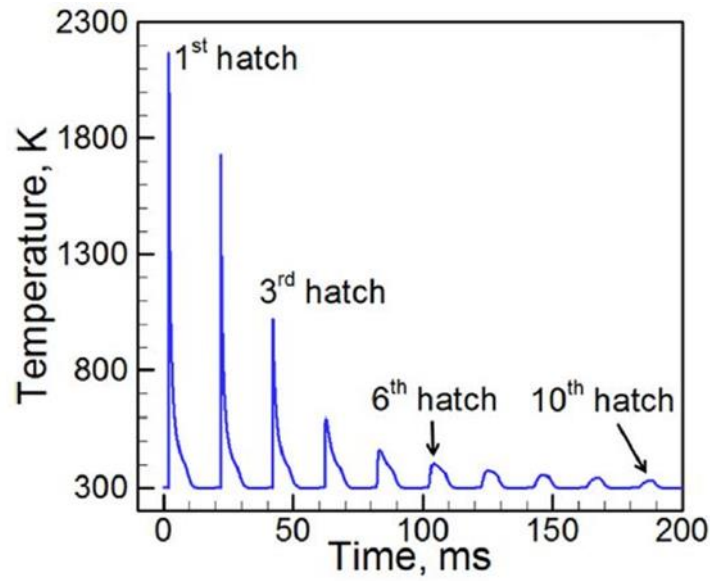
Figure 5. Effect of heat in 10 hatches, one layer build with scanning speed of 1000 mm/s and laser power of 60 W. Temperature is measured in track mid-length on the top surface of the first hatch. Other parameters are same as in table 1. (Mukherjee et al. 2018b, p. 372.)

It can be seen in figure 5 that as the laser beam moves towards the further hatches, the peak temperature at the measuring point decreases, as it can be assumed, because the laser beam goes further from the measuring point in each hatch (Mukherjee et al. 2018b, p. 372; Yang & Wang 2008, p. 1066). The temperature peaks decrease gradually and stabilize to the ambient temperature when the laser beam is far enough from the measuring point. The temperature provided from scanning of the second hatch is sufficient to re-melt the first hatch. (Mukherjee et al. 2018b, p. 372.) A corresponding model with three hatches and three layers build was also created by Mukherjee et al. (2018b, p. 372). This model describes the spatial effect of heat during a multi-hatch, multi-layer build. The measuring point of the thermal cycles is again in the track mid-length, on top surface of the first hatch in the first layer (see figure 4). (Mukherjee et al. 2018b, p. 372.) Thermal cycles are represented in figure 6.
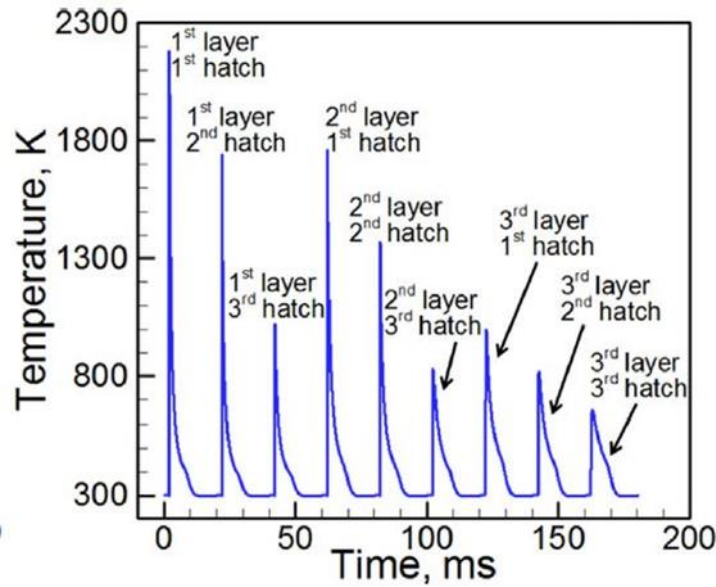
Figure 6. Effect of heat in three hatches, three layer build with scanning speed of 1000 mm/s and laser power of 60 W. Temperature is measured on the top surface in track mid-length of the first hatch of the first layer. Other parameters are same as in table 1. (Mukherjee et al. 2018b, p. 372.)

It can be seen in figure 6 that the planar thermal behavior is equal to the situation represented in figure 5. However, once the laser beam returns on top of the first hatch in order to build the second layer on top of the first layer, the measuring point experiences a new high temperature peak. The temperature peak of the first hatch of the second layer is sufficient to re-melt the already solidified lower layer locally. Again, the further the laser beam goes from the first layer in the building direction (z-axis), the lower the temperature peaks are. (Li et al. 2017, p. 164; Mukherjee et al. 2018b, p. 372; Yang et al. 2017, p. 608.) A single hatch may re-melt and solidify multiple times during the build, depending on the parameters and geometry of the part. A hatch will melt and solidify when exposed to laser beam but may re-melt and solidify again due to scanning of nearby hatches. Typically the layer beneath the surface is re-melted in L-PBF due to the reach of high intensity laser beam. (Li et al. 2017, p. 163-164; Mukherjee et al. 2018b, p. 372.)

The effect of heat in L-PBF was also studied by Yang et al. (2017). They created a model to predict temperature history of 4140 steel. The heat transfer depends on the local geometry which can be very complex in L-PBF but the geometry in this experiment was square (2.5

mm × 2.5 mm), because of simplicity. The unidirectional scanning pattern was rotated by 67° for each new layer. (Yang et al. 2017, p. 603-604.) The result is shown in figure 7.
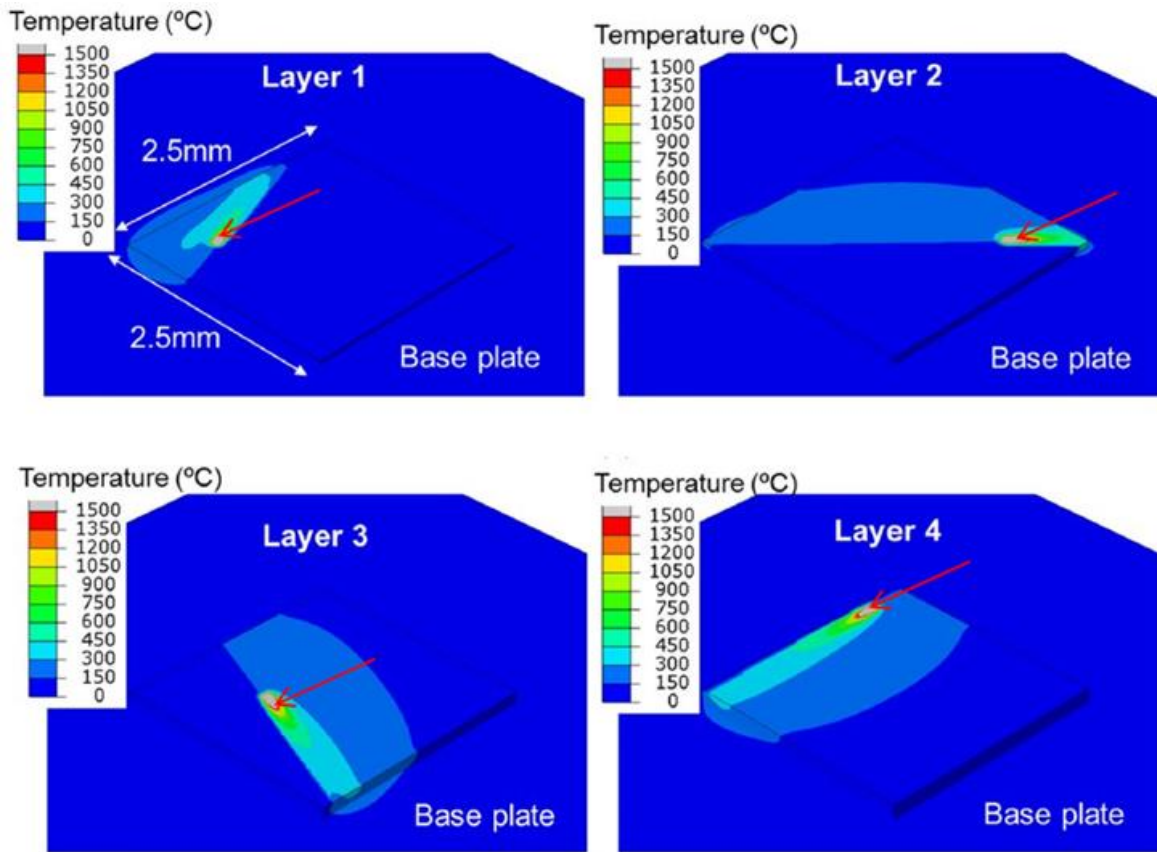

Figure 7. Effect of heat in L-PBF of 4140 steel. Laser power of 350 W and scanning speed of 867 mm/s were used. Melt pool region is represented in gray color. (Modified from Yang et al. 2017, p. 607.)

The effect of heat was plotted in four different stages of build (layers 1-4), as shown in figure 7. Gray color indicates the melt pool region (pointed with red arrow in figure 7). (Yang et al. 2017, p. 606-607.) It can be seen in figure 7 that heat spreads around the melt pool only to the already solidified area of the part because of its higher thermal conductivity compared to powder side that acts as an insulator (Mukherjee et al. 2018b, p. 373; Yang et al. 2017, p. 606-607). Figure 8 represents the thermal cycle experienced in the same experiment as figure 7 shows but specifically for layers 2, 4 and 6 (Yang et al. 2017, p. 608).
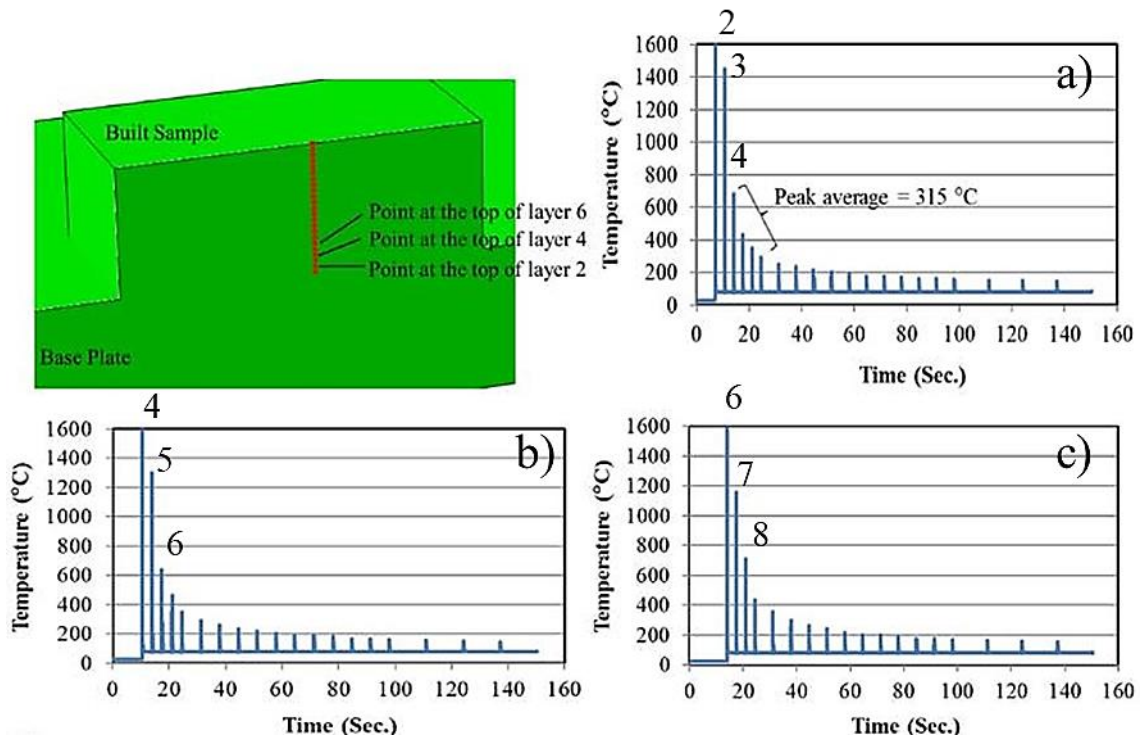
Figure 8. Thermal cycle measured on top surface in the middle of the (a) second, (b) fourth and (c) sixth layer. Laser power of 350 W and scanning speed of 867 mm/s were used. (Modified from Yang et al. 2017, p. 608.)

It can be noticed in figure 8 that the peak temperature is lower when more layers are built because the laser beam gets further from the measuring point as the build of part continues, which was noticed also in the studies of Li et al. (2017, p. 164) and Mukherjee et al. (2018b, p. 372) (Yang et al. 2017, p. 606). In addition to this observation, it can also be seen in figure 8 that the temperature peak of the previously scanned layer is lower as the build continues in upper layers. Temperature of the seventh layer, measured from the sixth layer, is in a range of 1150 °C (see in figure 8c) whereas the temperature of the third layer, measured from the second layer, is in a range of 1450 °C (see in figure 8a). Because this model in figure 8 describes how the heat conducts in the part during the build, this phenomenon could be explained due to the increase in volume of the part as the build proceeds which enables the heat to spread into larger volume, reducing the local temperature peaks near the surface. Accumulation of heat in the part cannot be observed in figure 8 as the temperature decreases continuously while proceeding in the upper layers. However, the global temperature of the part increases as the build proceeds because more heat is input to the part by every scanned

hatch and layer, according to Yang & Wang (2008, p. 1065-1066). The global temperature evolution is represented in figure 9.
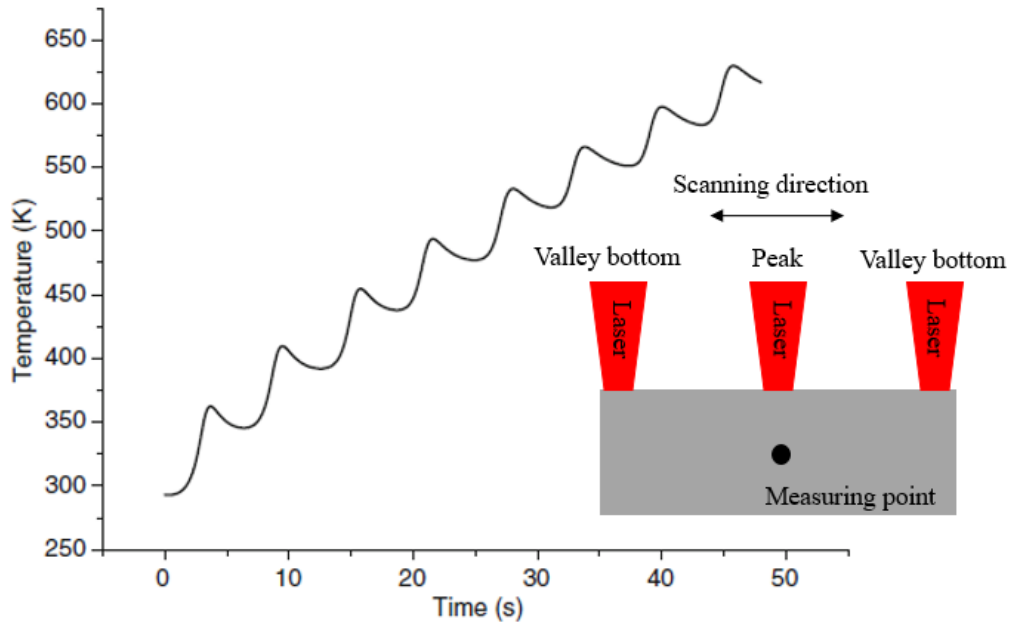

Figure 9. The temperature evolution of a $30 \times 2.4 \times 6.0$ mm block. Every peak indicates scanning of a new hatch. Temperature is measured in the center point of the block. (Modified from Yang & Wang 2008, p. 1065.)

As observed in figure 9, the temperature of the part increases gradually as the build proceeds which is known as accumulation of heat. Every peak observed in figure 9 indicates the moment when the laser beam scans in the track middle length at a location of few layers up from the measuring point, and every valley indicates the cooling of the hatch while laser beam is moving away from the track middle length. (Yang & Wang 2008, p. 1066.)

Based on figure 8, it can be noted that the area with highest temperature is the surface of the part, being nearest to the laser beam, and as the build continues to the upper layers, the temperature of that area decreases gradually because laser beam goes further from it after each layer until it reaches the ambient temperature (Yang et al. 2017, p. 606, 608). On the other hand, while the laser beam travels further from a specific layer to the upper layers, more heat is input to the part by every layer which increases the ambient temperature of the part, as seen in figure 9 (Yang & Wang 2008, p. 1065-1066).

2.2 Heat transfer

In L-PBF the heat transfers from the melt pool to its surroundings in different ways which are conduction, convection and radiation (Yang et al. 2017, p. 601). These heat transfer modes are represented in figure 10 (Masoomi et al. 2017, p. 74).
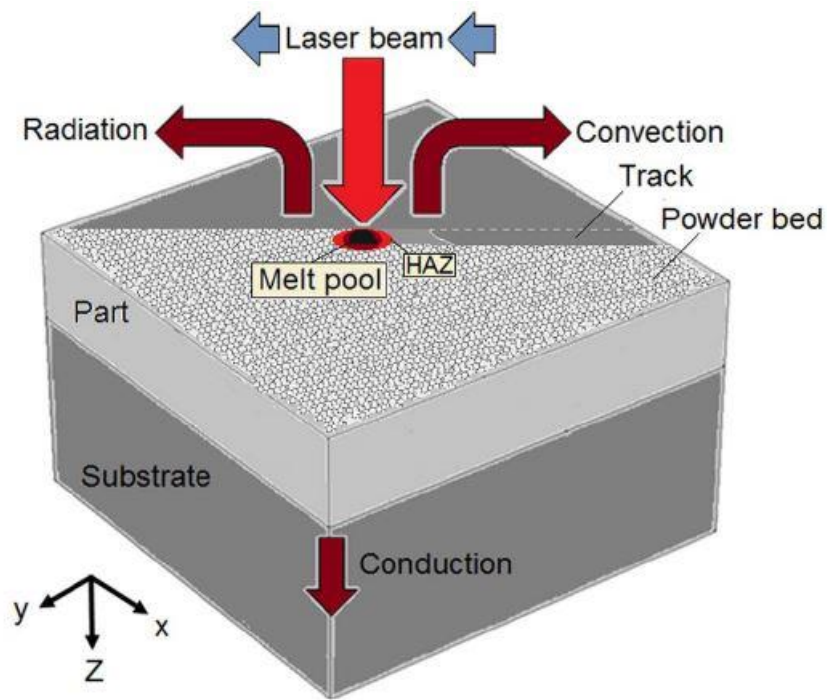

Figure 10. Modes of melt pool heat transfer in L-PBF including conduction, convection and thermal radiation (Masoomi et al. 2017, p. 74).

Heat transfers by convection within the liquid melt pool, by conduction within the solid material and by thermal radiation in both the liquid and solid state materials (Li et al. 2017, p. 161; Mukherjee et al. 2018a, p. 304). Also some of the laser energy is reflected from the surface of the powder bed due to the lustrous nature of metals. The heat transfer by thermal radiation is still minor compared to the other heat transfer modes. (Yang et al. 2017, p. 601.)

The primary heat transfer direction via conduction from the melt pool to its surroundings changes continuously during the build in a multi-layer and multi-hatch builds because there are varying surroundings for the melt pool in different stages of build (Ilin et al. 2014, p. 398-399; Mukherjee et al. 2018b, p. 373). These surroundings are represented in figure 11 (Mukherjee et al. 2018b, p. 373).
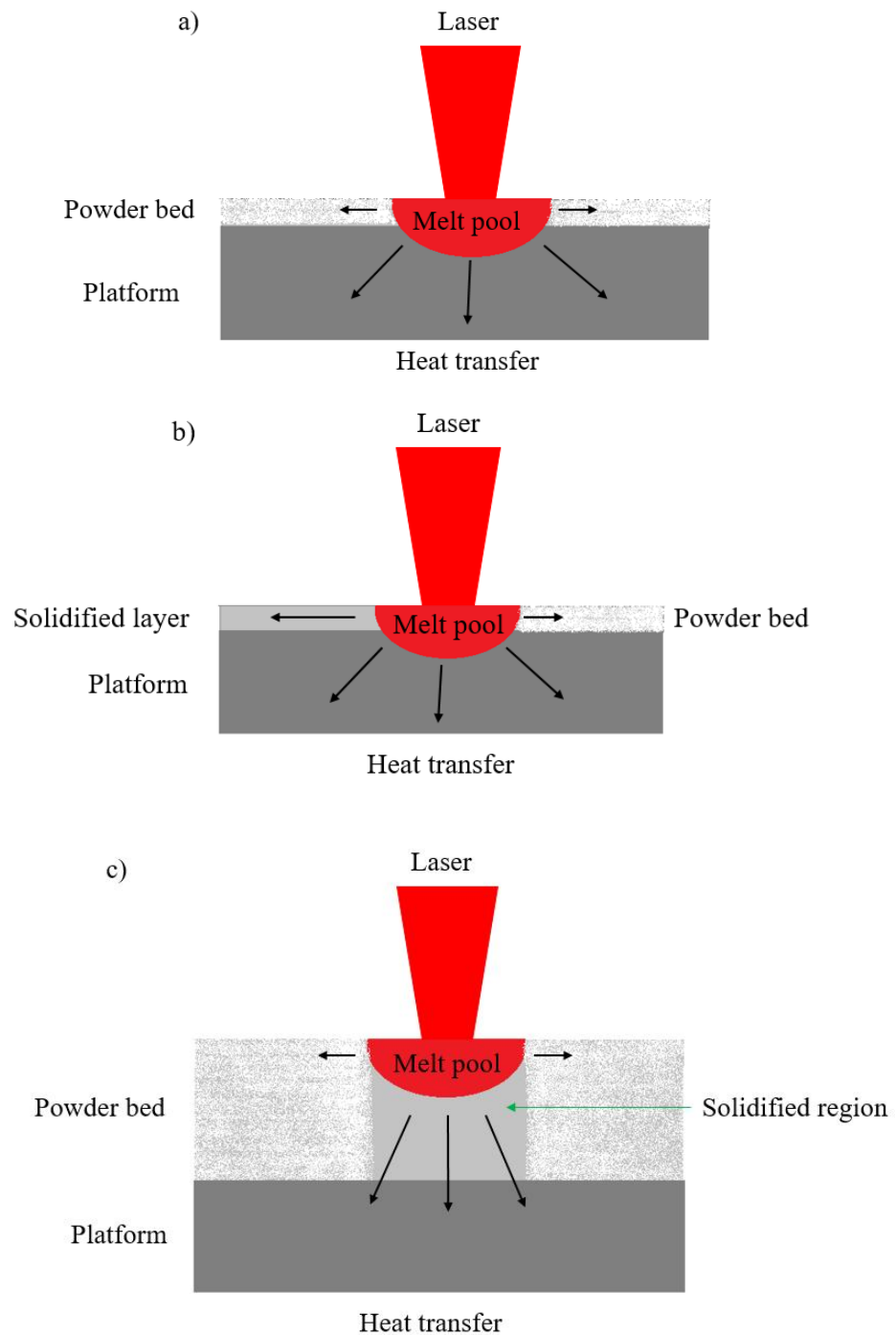
Figure 11. Surroundings of the melt pool in different stages of build and primary heat transfer direction in these stages (length of the heat transfer arrow indicates its magnitude). Reportedly, laser beam is transmitted perpendicularly to the powder bed. (Modified from Mukherjee et al. 2018b, p. 373.)

The melt pool is surrounded by powder from both sides in the beginning of the build, especially in the first hatch (see figure 11a). The primary heat transfer direction in that

situation is towards the platform because of its higher thermal conductivity compared to powder bed. The melt pool is surrounded by powder from one side and by solid material on the other in the second and further hatches of the layer. Solid material has higher thermal conductivity than powder and therefore the primary heat transfer direction in that situation is towards the already solidified hatches and the platform, like shown in figure 11b. When proceeding in the build to the first hatch of the next layer, the melt pool is again surrounded by powder from both sides. However, melt pool has now already deposited solid layers underneath it, through which the primary heat transfer goes all the way to the platform, like shown in figure 11c. Distance from melt pool to the platform increases when number of built layers increases. Meanwhile the heat transfer from the highest layer to the platform is smaller as some of the heat will remain in the part. (Mukherjee et al. 2018b, p. 373.) When the heat is continuously supplied to the growing part and the distance from top layer to the substrate grows, the heat starts to accumulate in the part, which may cause defects (Mukherjee et al. 2018b, p. 373; Yang & Wang 2008, p. 1065-1066).

Thermal conductivity is essential matter in L-PBF as it affects the accumulation of heat in the part during the build. Lower thermal conductivity results in larger melt pool and higher temperatures of the build. (Ilin et al. 2014, p. 399; Mukherjee et al. 2018a, p. 306-307.) Thermal conductivity is material related property but it can be slightly tuned by parameters such as powder packing efficiency and powder particle size. Thermal conductivity of a powder bed that consists of inert gas such as argon and SS 316 powder increases with the increase in temperature because thermal conductivity of both SS 316 powder and argon gas increase with increase in temperature. Higher powder packing efficiency enables higher thermal conductivity of the powder bed. The powder particles share larger area of contact per unit volume (specific surface area) with higher powder packing efficiency, facilitating the heat transfer between the particles, which results in higher thermal conductivity of the powder bed. Also, smaller particle size results in higher thermal conductivity of the powder bed. Smaller particle size reduces the inter particle space for shielding gas, leaving less room for shielding gas in the powder bed. Because shielding gas has lower thermal conductivity than metal powder, this results in higher thermal conductivity of the powder bed. Smaller particles also have larger specific surface area that improves thermal conductivity of the powder bed. (Mukherjee et al. 2018a, p. 306-307.)

Different surroundings of the melt pool, which are represented in figure 11, affect the melt pool volume in L-PBF of SS 316. Mukherjee et al. (2018b, p. 374) created a model to predict the melt pool volume in different stages of build. The melt pool volume in this model was measured at third hatch for five subsequent layers and at third layer for five subsequent hatches (Mukherjee et al. 2018b, p. 374). The results are shown in figure 12.
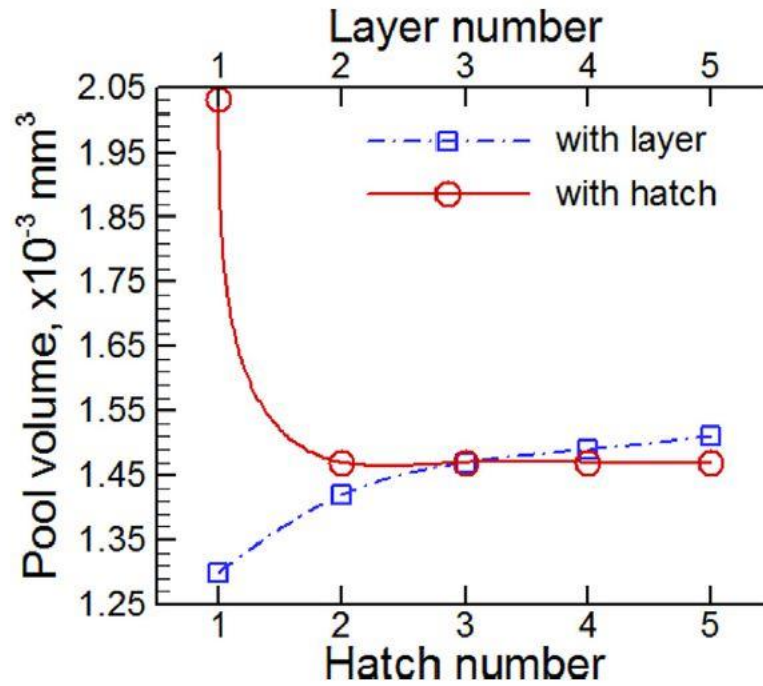

Figure 12. Melt pool volume for five subsequent hatches in third layer and for third hatch in five subsequent layers. Measured on top surface, in the mid-length of the track. Scanning speed of 1000 mm/s and laser power of 60 W were used. Other parameters are the same as in table 1. (Mukherjee et al. 2018b, p. 374.)

It can be seen in figure 12 that melt pool volume increases (blue graph) with increasing number of layers. As more layers are built, heat will eventually accumulate in the part and increase the part temperature which leads to larger melt pool and reduced cooling rate of the melt pool (Ilin et al. 2014, p. 396; Mukherjee et al. 2018b, p. 374). However, melt pool volume decreases remarkably after the first hatch of a layer (red graph) and melt pool volume remains nearly stable for the following hatches of the layer (see in figure 12). Melt pool volume decreases and stabilizes after the first hatch because the second and further hatches of the layer have solid material on the other side that has higher thermal conductivity. Thus, heat is effectively transferred through the solid side. Melt pool is surrounded by powder in

both sides in the first hatch and this causes larger melt pool due to low thermal conductivity of surrounding powder. (Mukherjee et al. 2018b, p. 373-374.)

2.3 Cooling rate

The part goes through repeating cycles of heating and cooling during the build in L-PBF. The excessive heat must be transferred out of the part as effectively as possible in order to ensure a successful build. (Masoomi et al. 2017, p. 73-74; Yang et al. 2017, p. 599.) Mukherjee et al. (2018b, p. 376-377) modeled a five hatches, five layer build with cooling rates. Cooling rates are measured at third hatch for five subsequent layers and at third layer for five subsequent hatches (Mukherjee et al. 2018b, p. 377). This is shown in figure 13.
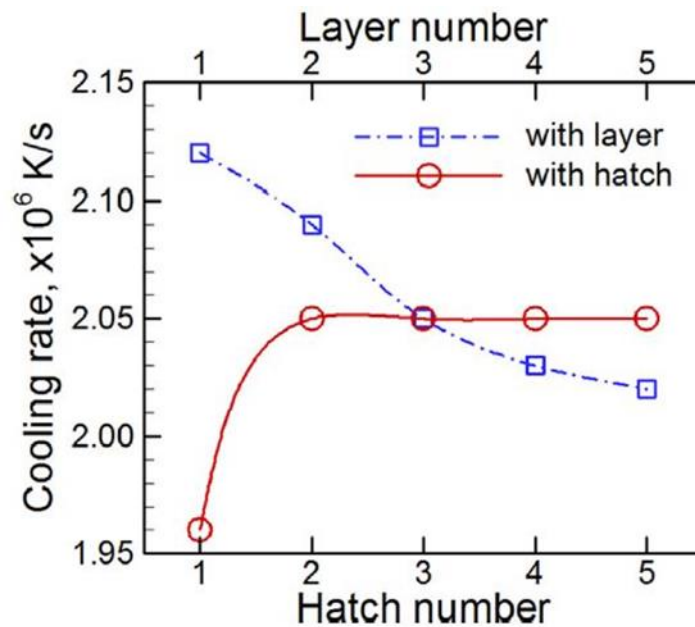

Figure 13. Cooling rates for five subsequent hatches in third layer and for third hatch in five subsequent layers. Measured on top surface, in the mid-length of the track. Scanning speed of 250 mm/s and laser power of 60 W were used. Other parameters are same as in table 1. (Mukherjee et al. 2018b, p. 377.)

As figure 13 illustrates, upper layers of the build have lower cooling rates (blue graph). This occurs because the heat will accumulate into the part during the build and as the build proceeds for higher layers, the temperature of the part increases, which causes reduced cooling rate (Mukherjee et al. 2018b, p. 376; Yang & Wang 2008, p. 1065-1066). Also melt pool size increases when proceeding for upper layers in the build, as observed in figure 12.

Larger melt pool cools down slower than smaller one due to higher volume (Bertoli et al. 2017, p. 391; Mukherjee et al. 2018b, p. 375). Then again, the first hatch of the layer has the lowest cooling rate because of powder being on both sides of the melt pool. This disables effective heat transfer and also leads to larger melt pool as observed in figure 12. After the first hatch, the cooling rate increases because one side of the melt pool is solid material that has higher thermal conductivity than powder. For the following hatches of the layer, cooling rate remains stable, as shown in figure 13 (red graph). (Mukherjee et al. 2018b, p. 376.) Based on figures 12 and 13, it can be stated that melt pool volume and cooling rate are dependent on each other, and they are affected by temperature of the build. Shortly, higher temperature causes larger melt pool and lower cooling rate.

Parameters such as scanning speed, laser power, layer thickness and hatch spacing affect the cooling rate of the part (Mukherjee et al. 2018b, p. 376-377). Higher scanning speeds go through the scanning lines faster and amount of heat input is smaller to the part. Because of lower heat input per unit length with high scanning speeds, the melt pool is smaller compared to lower scanning speed accompanied melt pools. Smaller melt pool cools down and solidifies quicker than larger one. (Bertoli et al. 2017, p. 391; Ilin et al. 2014, p. 394; Mukherjee et al. 2018b, p. 375.) An increase in laser power results in decrease in cooling rate because more heat is input to the part (Bertoli et al. 2017, p. 391). Higher layer thickness results in lower cooling rate because of the combination of higher absorptivity of heat and lower heat transfer through thicker powder layer. As long as subsequent hatches overlap each other sufficiently, cooling rate remains nearly constant but when the hatches are too far away from each other, the surroundings of the melt pool consist more of powder. This causes reduction in the cooling rate and insufficient fusion. (Mukherjee et al. 2018b, p. 377.)

2.4 Thermal stress

Subsequent rapid melting and solidification of powder in L-PBF is the nature of the process and it sets challenges in manufacturing as deformations in parts may occur due to thermal stresses (Kruth et al. 2004, p. 617; Masoomi et al. 2017, p. 73-74; Yang et al. 2017, p. 599). Response of metal to the local temperature changes is to expand or contract whether heated or cooled, respectively, and when expansion or contraction of metal is restricted, thermal stresses occur (Simson et al. 2017, p. 184-185).

The generation of thermal stresses can be explained with temperature gradient mechanism (TGM) and cool-down mechanism (Kruth et al. 2004, p. 617; Simson et al. 2017, p. 185). TGM is illustrated in figure 14 (Li et al. 2015, p. 709).
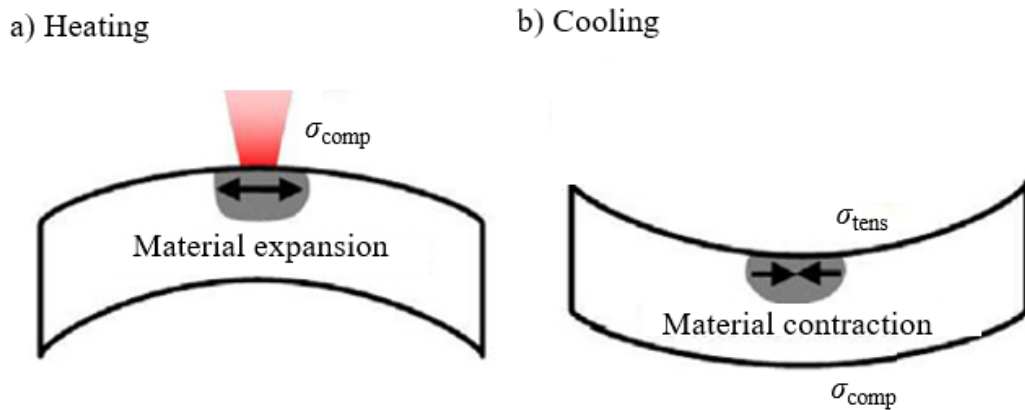

a) Heating b) Cooling

σ_{comp}

Material expansion

σ_{tens}

Material contraction

σ_{comp}

Figure 14. Schematic of the TGM (modified from Li et al. 2015, p. 709).

When the laser beam interacts with powder bed, the powder melts and the surface of the part is strongly heated. During this heating cycle, surface of the part pursues to expand due to strong heating but the expansion of the heated top layer is limited due to surrounding solid material, which creates compressive stress σ_{comp} on the upper surface, as seen in figure 14a. When the occurred compressive stress exceeds yield strength of the material, the top surface will have plastic deformation that pursues to upset the material towards the laser, like shown in figure 14a. When cooling of the material begins, the material starts to contract. Now contraction of the surface is limited due to surrounding solid material, which ends up in tensile stress σ_{tens} on the top surface. When the tensile stress exceeds yield strength of the material, the top surface pursues to bend into the opposite direction like shown in figure 14b. (Kruth et al. 2004, p. 617-618; Simson et al. 2017, p. 185.) Additional stresses are created only below the melting point which means that TGM does not require melting of the material (Kruth et al. 2004, p. 617; Mercelis & Kruth 2006, p. 255).

One important function of the support structures in L-PBF is to anchor the part to the building platform and to prevent the part from warping during the build, in the presence of the stresses. However, the resistance for warping gains residual stress in the part. Support structures also have an important role in conducting the heat away from the part by transferring the heat towards the building platform. (Liu, Yang & Wang 2016, p. 654.)

Higher temperature of the part lowers the yield strength of the material which increases its vulnerability to have deformations (Kruth et al. 2004, p. 617). The more heat is input to the part, the more residual stress it will gain. This means that by each new scanned layer, more stresses are generated (Mercelis & Kruth 2006, p. 259). Schematic of cool-down mechanism is illustrated in figure 15 (Simson et al. 2017, p. 185).
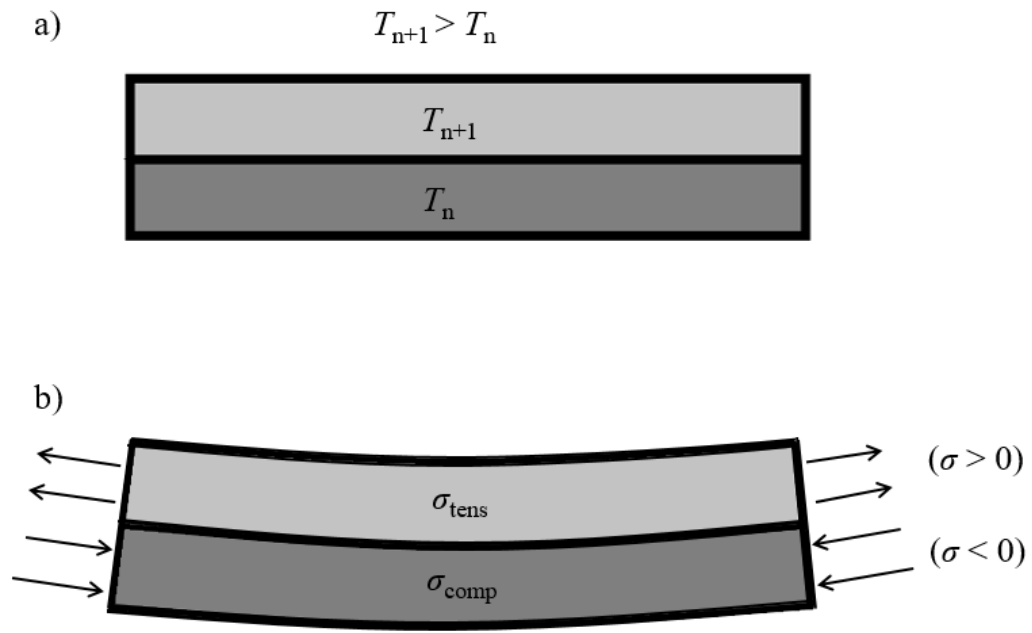
a) $T_{n+1} > T_n$

T_{n+1}

T_n

b)

σ_{tens}

σ_{comp}

$(\sigma > 0)$

$(\sigma < 0)$

Figure 15. Schematic of the cool-down mechanism (modified from Simson et al. 2017, p. 185).

Figure 15a illustrates that the heated top layer T_{n+1} has higher temperature compared to the layer beneath it T_n and when the top layer solidifies and cools down, it contracts more than the layer beneath it. As the layers are melted and solidified strongly together in the process, presence of the lower layer limits the contraction of the upper layer, which results in tensile stress in the upper layer and compressive stress in the lower layer (see figure 15b). (Mercelis & Kruth 2006, p. 255; Simson et al. 2017, p. 185.) TGM and cool-down mechanism work globally in the part, meaning that the residual stresses and deformations occur in x-, y- and z-directions, not only in certain direction (Li et al. 2015, p. 709-711).

2.5 Residual stress and deformation

Yang et al. (2017) have modeled a solid block to demonstrate the residual stresses derived from L-PBF and a bridge sample to demonstrate the deformation behavior of metal parts.

The material used in these simulations was Inconel 718 and parameters used in the build and the model, are represented in table 2 (Yang et al. 2017, p. 605, 607).

Table 2. Parameters used in the model and the build of a block and a bridge sample (Yang et al. 2017, p. 607).

Laser power	285 W
Scanning speed	960 mm/s
Focal point diameter	100 µm
Layer thickness	40 µm
Scanning strategy	Unidirectional, rotated 67° for each layer
Material	Inconel 718

Figure 16 represents the predicted maximum principal stress distributions in the block model. The model is a cross-sectional view, enabling to see the stresses inside the block. (Yang et al. 2017, p. 613.)
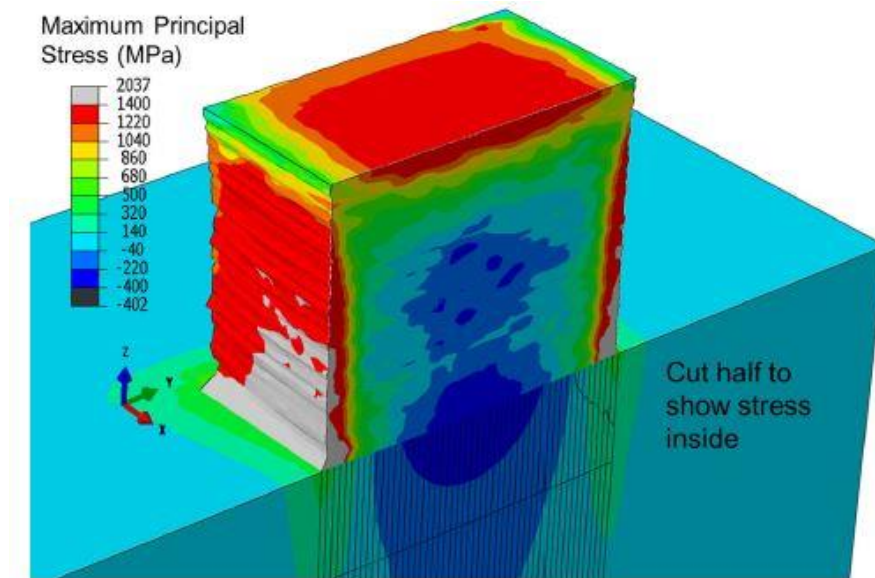
Figure 16. Cross-sectional view of the Inconel 718 block including maximum principal stresses. Scanning speed of 960 mm/s and laser power of 285 W were used. Other parameters are same as in table 2. (Yang et al. 2017, p. 613.)

As it can be observed in figure 16, compressive stress σ_{comp} dominates inside the block whereas tensile stress σ_{tens} locates on the outer surface of the block, which obeys the TGM

and cool-down mechanism. The highest stress value can be obtained in the lower corners of the block that are attached to the building platform (grey area), acting tensile stress. High tensile stress values (appear in red in figure 16) are obtained only at surface, not extending deep inside the block. (Mercelis & Kruth 2006, p. 256-257; Yang et al. 2017, p. 611.) Compressive stress reaches inside the building platform in addition to the block itself, exposing the upper section of the building platform in compressive stress and the lower section of the building platform in tensile stress (Mercelis & Kruth 2006, p. 257). The tensile stress values appear higher than compressive stress values in figure 16. Based on the residual stresses in figure 16, possible deformation in which the edges of the block would rise from the building platform, could be observed at the highest tensile stress area in the lower corners of the block (indicated with grey color). The bridge sample used to demonstrate the deformations in the study of Yang et al. (2017) is represented in figure 17.
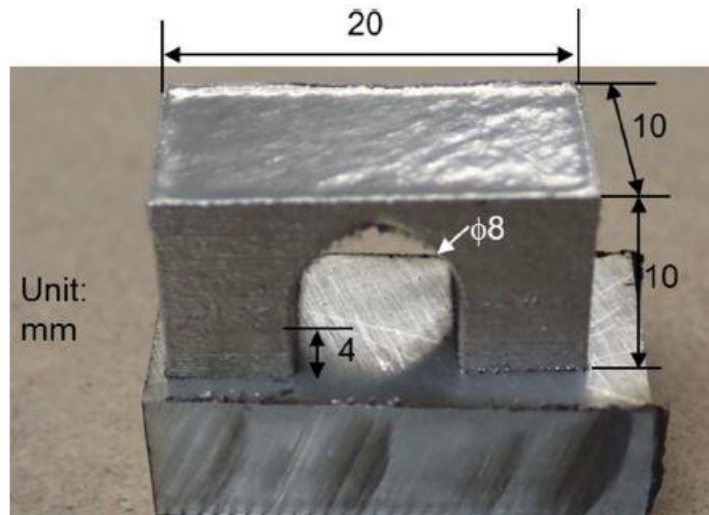

Figure 17. As built bridge sample and its dimensions. Laser power of 285 W and scanning speed of 960 mm/s were used. Other parameters are same as in table 2. (Yang et al. 2017, p. 606-607.)

Figure 18 represents the predicted deformation magnitudes of the bridge sample in building direction (z-axis) and predicted deformation shape, magnified by five in order to enhance the visualization of the deformations (Yang et al. 2017, p. 612-613).
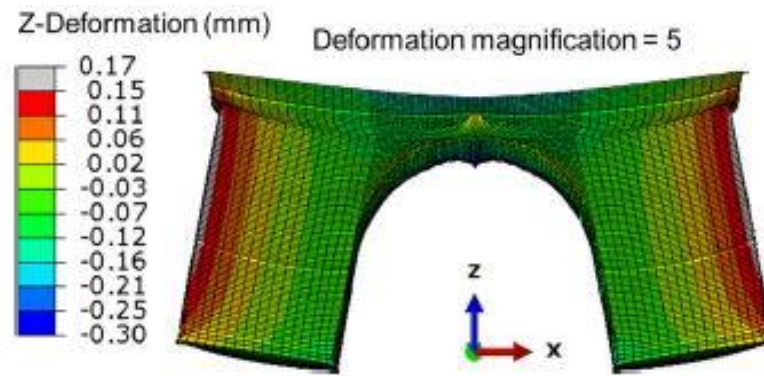
Figure 18. Predicted deformation magnitudes in building direction (z-axis) and exaggerated deformation shape of the bridge sample (Yang et al. 2017, p. 613).

It can be seen in figure 18 that the original flat surface on top of the bridge is bent down in the middle and bridge legs have spread and raised, due to the residual stresses caused by cyclic heat that is inherent in L-PBF (Yang et al. 2017, p. 612-613). The manufactured bridge sample after removing from building platform, is represented in figure 19 (Yang et al. 2017, p. 614).
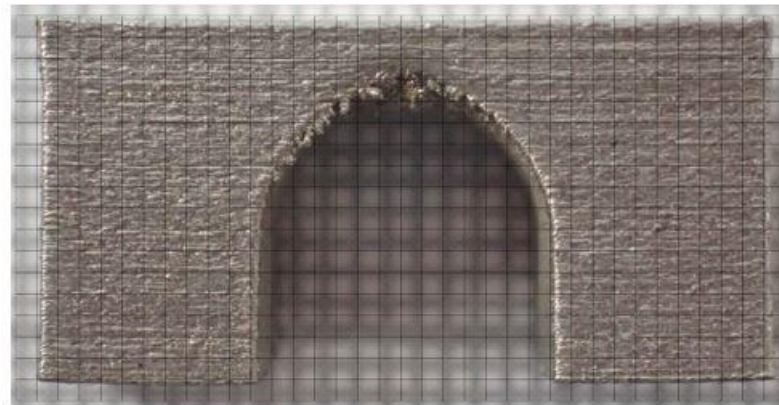
Figure 19. The bridge sample after removing form building platform. Grid is added to clarify the deformations. (Yang et al. 2017, p. 614.)

The predicted deformations represented in figure 18 exist also in the actual part, as seen in figure 19. The deformations look smaller in the part because in the model they were magnified by five in order to enhance the visualization of the results. The original flat surface on top of the bridge is bent down in the middle and the legs of the bridge are spread, as the model predicted in figure 18. (Yang et al. 2017, p. 612-614.) The measures of deformations in the building direction (z-axis) on top surface of the bridge sample are represented in figure

20. Deformation zero-point is in the middle of the top surface. (Yang et al. 2017, p. 612-614.)
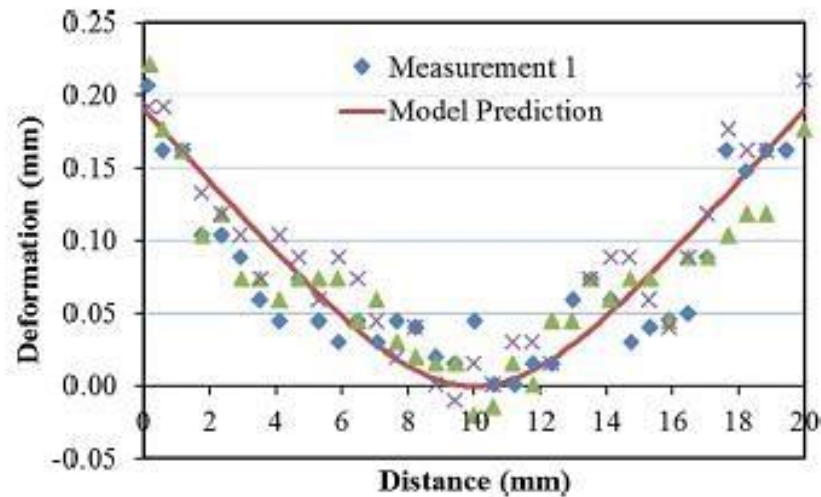

Figure 20. Deformation in the building direction (z-axis) on top surface of the bridge sample (Yang et al. 2017, p. 614).

It can be seen in figure 20 that the outer corners of the bridge are c. 0.19 mm higher than the middle point of the bridge, according to the model. The measurement follows the same slope as the prediction. (Yang et al. 2017, p. 613-614.) This deformation shape complies with the TGM and cool-down mechanism.

Also in the study of Wu et al. (2014), deformations induced by cyclic heat in L-PBF were examined. Wu et al. (2014) used a prism shape to demonstrate the deformations occurred in SS 316L parts. Parameters used in the study are represented in table 3.

Table 3. Parameters used in the study of Wu et al. (2014, p. 6261, 6263).

Laser power	400 W
Scanning speed	1800 mm/s
Focal point diameter	50 µm
Layer thickness	30 µm
Scanning strategy	5×5 mm islands
Material	SS 316L

Geometry and dimensions of the test samples and their orientation on the building platform are shown in figure 21 (Wu et al. 2014, p. 6262).
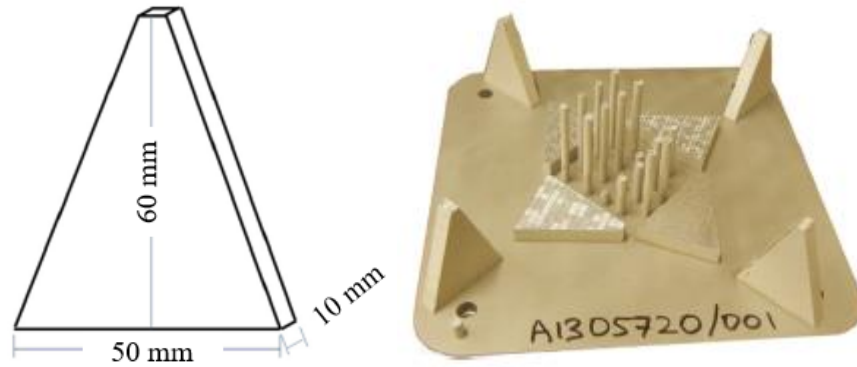

Figure 21. Geometry and dimensions of the test samples and orientation on the building platform (modified from Wu et al. 2014, p. 6262).

Samples were built both horizontally and vertically with parameters shown in table 3. Deformations occurred during the removal of the samples from the building platform, when the residual stresses released and resulted in deformations (Wu et al. 2014, p. 6264-6265). Deformations of the horizontally built samples in x-, y- and z-axis are represented in figure 22 (Wu et al. 2014, p. 6264).
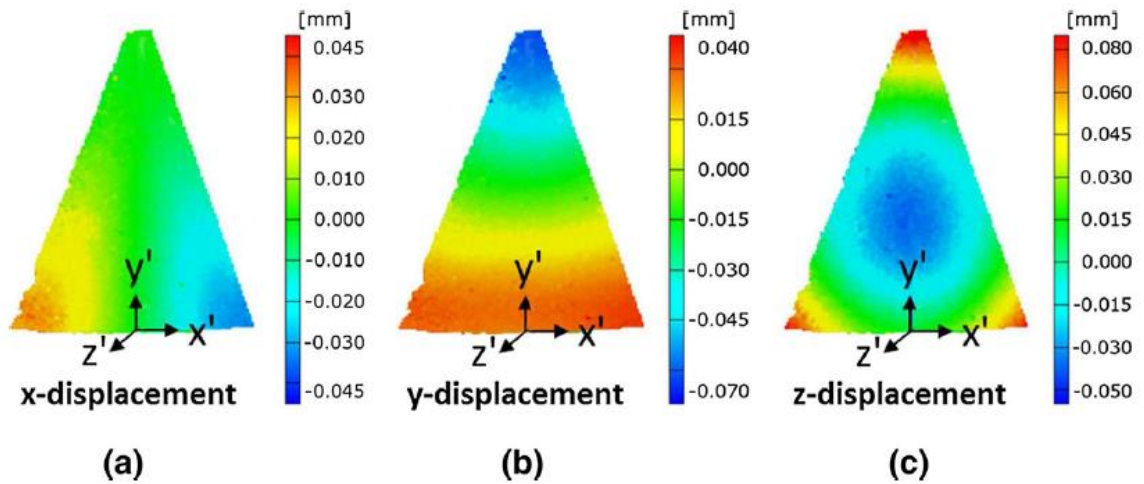

Figure 22. Deformation magnitudes of the horizontally built test samples in (a) x-, (b) y- and (c) z-axis, represented in a local coordinate system and measured on top surface. Local z-axis indicates building direction. Laser power of 400 W and scanning speed of 1800 mm/s were used. Other parameters are same as in table 3. (Wu et al. 2014, p. 6264.)

It can be seen in figure 22a that the displacement in x-axis locates in the lower corners of the prism, being equal on both sides (maximum 0.045 mm). The corners have contracted towards the center of the prism. Displacement in y-axis in figure 22b can be observed in the bottom and top regions of the prism, again contracting them towards the center of the prism. It can be noted that displacement of the top region (0.070 mm) is higher compared to the displacement of the bottom region (0.040 mm). (Wu et al. 2014, p. 6264-6265.) This can be explained due to the higher heat input in the smaller top region that has shorter cooling time compared to the larger bottom region of the prism (Kruth et al. 2004, p. 617). Displacement in z-axis in figure 22c describes the deformation in building direction. It can be observed in figure 22 that the prism has spherically deflected in a way that the corners of the prism have bent upwards (0.080 mm) while the center of the prism has bent downwards (0.050 mm). (Wu et al. 2014, p. 6264-6265.) Figure 23 illustrates exaggerated view of the total deformation shape of the horizontally built prism sample (Wu et al. 2014, p. 6264).
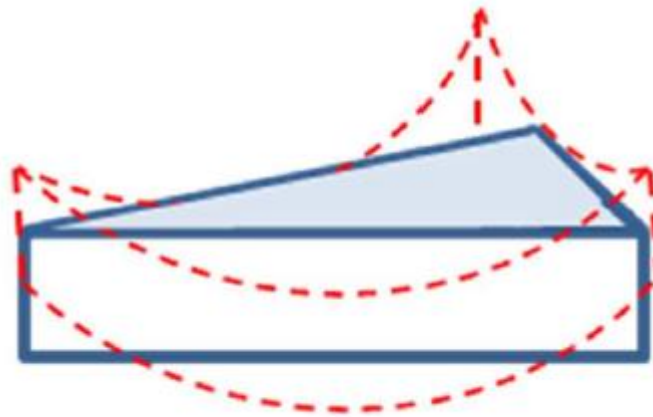

Figure 23. Exaggerated total deformation shape of the horizontally built prism sample (Wu et al. 2014, p. 6264).

The overall deformation shape represented in figure 23 obeys the TGM and cool-down mechanism. Deformations of the vertically built samples in x-, y- and z-axis are represented in figure 24 (Wu et al. 2014, p. 6264).
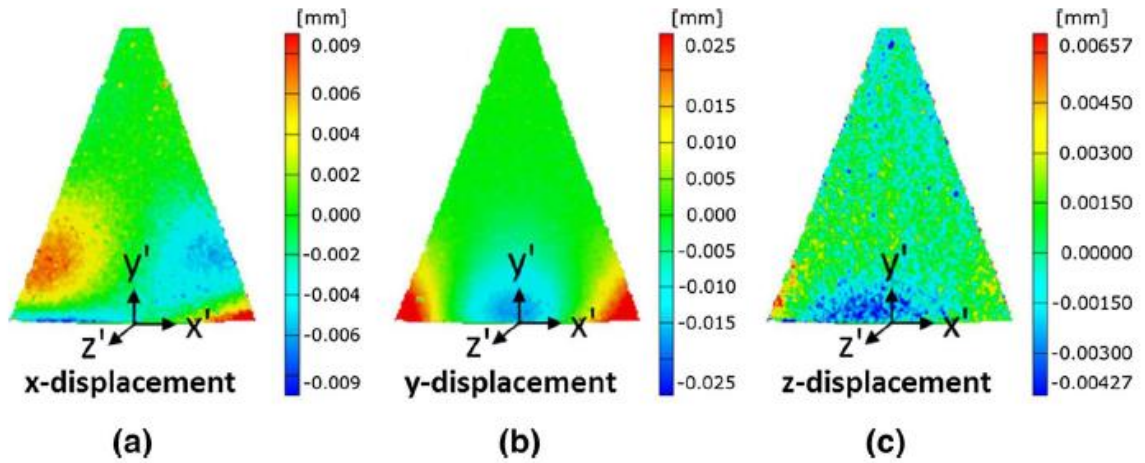
Figure 24. Deformation magnitudes of the vertically built test samples in (a) x-, (b) y- and (c) z-axis, represented in a local coordinate system and measured at side surface. Local y-axis indicates building direction. Laser power of 400 W and scanning speed of 1800 mm/s were used. Other parameters are same as in table 3. (Wu et al. 2014, p. 6264.)

It can be seen in figure 24a that the displacement in x-axis locates in the bottom region of the prism, more specifically at the sides of the prism just above the bottom corners, and acts contractive (0.009 mm). Displacement in y-axis in figure 24b describes the deformation in building direction and it locates in the bottom corners that have bent upwards (0.025 mm) while the middle bottom region has rounded (0.025 mm). Displacement in z-axis in figure 24c is minor compared to the x- or y-axis displacements and it locates in the bottom of the prism. (Wu et al. 2014, p. 6264-6265.) Based on figures 22 and 24, it can be noted that the largest deformations occur in the building direction and when it comes to horizontal plane, larger deformation occurs along the longer side of the part. It also appears that horizontal building orientation induces larger deformation than vertical building orientation, as it can be seen when comparing the deformation magnitudes of the prism sample between figures 22 and 24. Figure 25 represents exaggerated view of the total deformation shape of the vertically built prism sample (Wu et al. 2014, p. 6264).
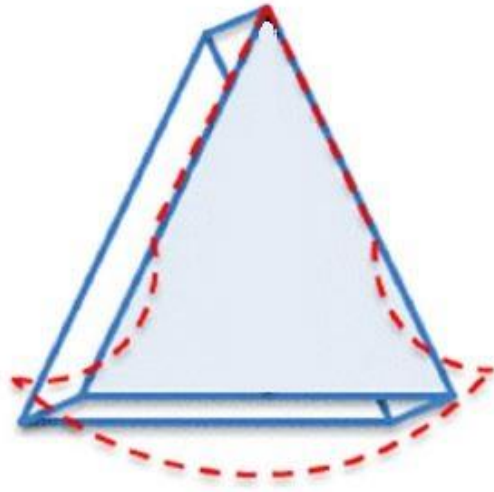
Figure 25. Exaggerated total deformation shape of the vertically built prism sample (modified from Wu et al. 2014, p. 6264).

It can be seen in figure 25 that the deformation shape of the vertically built sample is different compared to the deformation shape of the horizontally built sample represented in figure 23. The residual stresses induced by TGM pursue to lift the edges of part from the building platform, as seen in figures 23 and 25. Therefore, the deformation shape varies depending on the building orientation of the part.

Deformations of metal parts in L-PBF were also studied by Li et al. (2017). They created a model to predict residual stresses and deformations of a twin cantilever made of aluminum. Parameters used in the study are shown in table 4 and the geometry of the sample and its deformation is illustrated in figure 26 (Li et al. 2017, p. 159).

Table 4. Parameters used in the study of Li et al. (2017, p. 159).

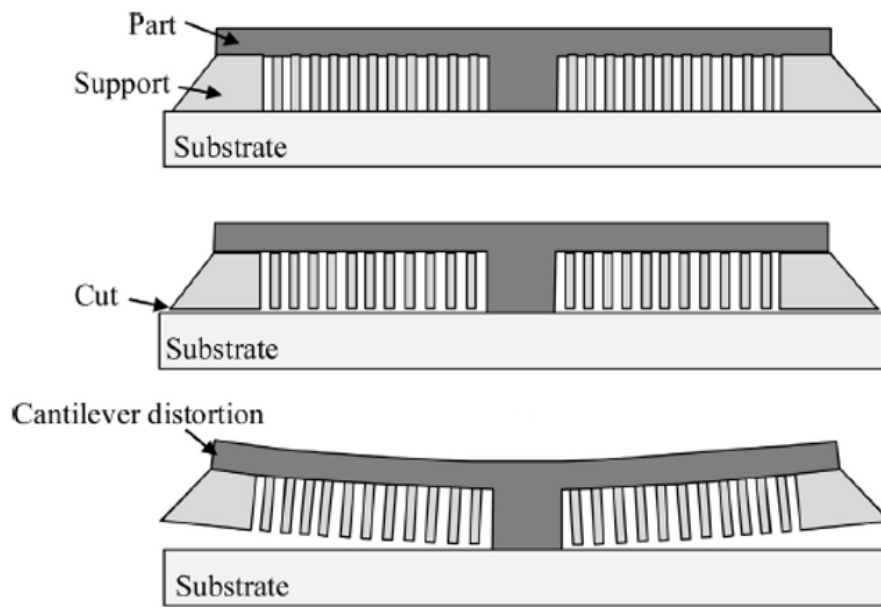| Laser power	195 W
Scanning speed	800 mm/s
Focal point diameter	100 µm
Layer thickness	30 µm
Scanning strategy	Unidirectional, rotated 67˚ for each layer
Material	AlSi10Mg

Figure 26. Schematic of a cantilever deformation (modified from Li et al. 2017, p. 159).

It can be seen in figure 26 that deformations occur after the support structures have been cut from the building platform, enabling the residual stresses to release, resulting in deformation of the part (Le Roux et al. 2018, p. 325; Li et al. 2017, p. 165; Mercelis & Kruth 2006, p. 263-264). The deformation obeys the TGM and cool-down mechanism. Figure 27 shows the cantilevers made of different thicknesses (after cutting the support structures) (Li et al. 2017, p. 159).
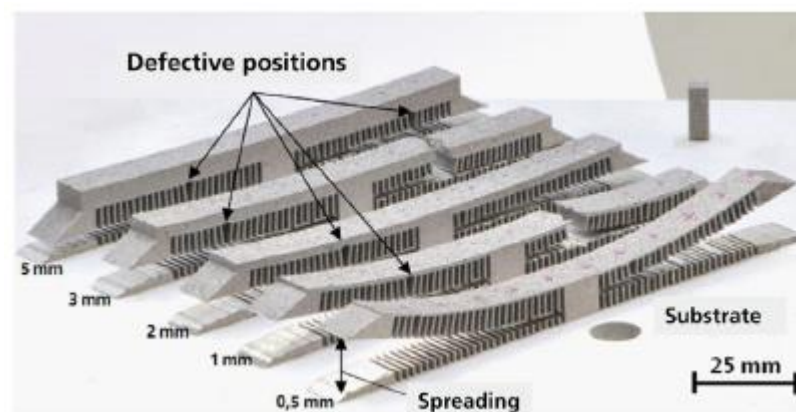

Figure 27. Deformations of cantilevers after cutting the support structures (Li et al. 2017, p. 159).

Based on figure 27, the thinnest cantilever arm (0.5 mm) shows the greatest deformation while the thickest arm (5.0 mm) shows the least deformation (Li et al. 2017, p. 159). The thinner areas have lower strength due to less material involved and therefore they have more deformation than areas with higher amount of material. Cantilever with 3.0 mm arm thickness was chosen for the simulation in the study of Li et al. (2017, p. 159). Residual stresses of the cantilever after build are represented in figure 28 (Li et al. 2017, p. 165).
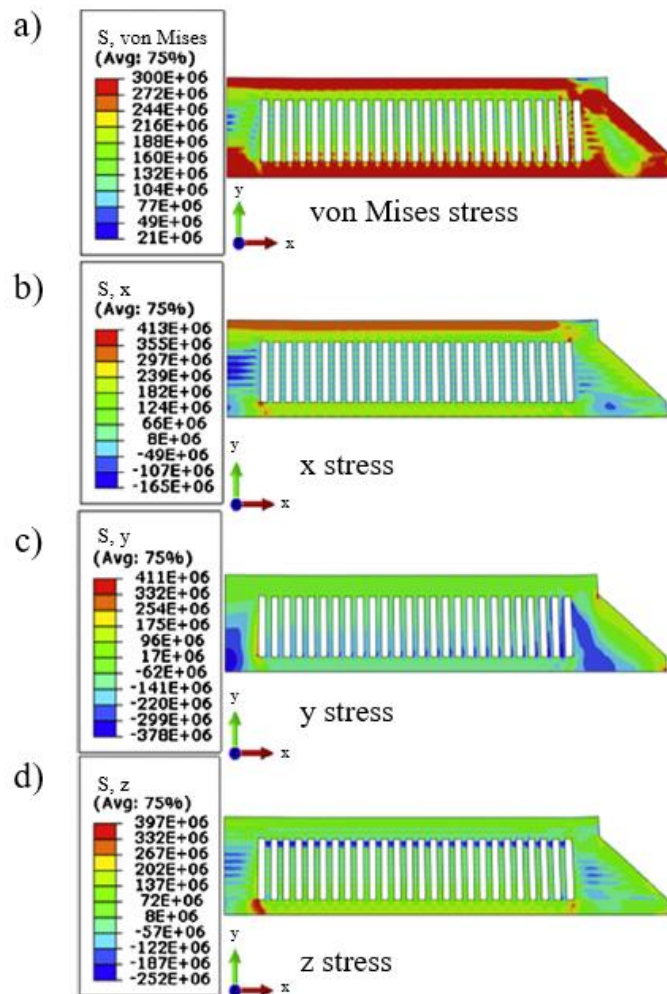

Figure 28. Residual stresses of the cantilever after build while still being attached to the building platform. Cross-sectional view of the half piece. Laser power of 195 W and scanning speed of 800 mm/s were used. Other parameters are same as in table 4. (Modified from Li et al. 2017, p. 165.)

It can be seen in figure 28b that tensile residual stress dominates in the part along x-axis and locates in the top surface of the cantilever arm, which obeys the TGM and cool-down

mechanism (Li et al. 2017, p. 165; Mercelis & Kruth 2006, p. 256-257). Tensile residual stress acts higher than compressive stress locally along z-axis also as seen in figure 28d. Compressive residual stress dominates along the building direction (see figure 28c) and locates in the end and middle regions of the cantilever. Overall von Mises stress in figure 28a is at its highest in the top surface and in the connection region of the part and the platform. (Li et al. 2017, p. 163, 165.) Figure 29 represents the corresponding data for situation when the support structures have been cut from the building platform (Li et al. 2017, p. 165).
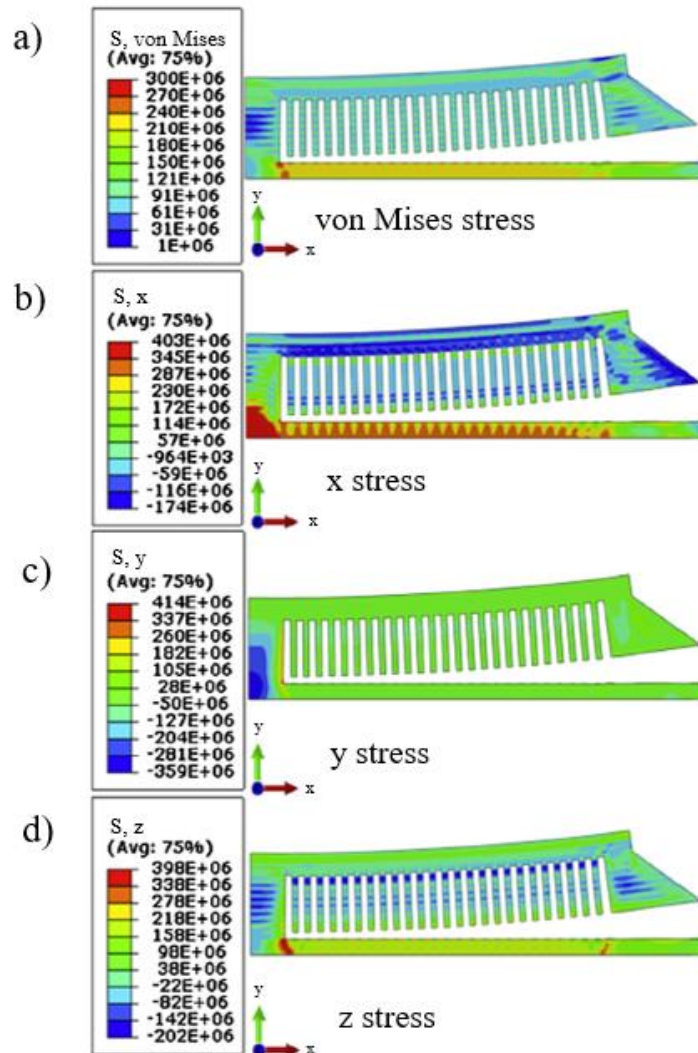

Figure 29. Residual stresses of the cantilever with support structures cut from the building platform. Cross-sectional view of the half piece. Laser power of 195 W and scanning speed of 800 mm/s were used. Other parameters are same as in table 4. (Modified from Li et al. 2017, p. 165.)

It can be noted in figure 29b that after cutting the support structures from the building platform, the tensile residual stress along x-axis on the top surface of the cantilever becomes compressive due to the plastic deformation of the cantilever arm (Li et al. 2017, p. 165). Overall von Mises stress in figure 29a dropped significantly after cutting the support structures as the stress relieved via deformation of the part (Li et al. 2017, p. 165; Mercelis & Kruth 2006, p. 256-257). The high von Mises stress remained only in the leg of the cantilever that was still attached to the building platform (Li et al. 2017, p. 163, 165). No significant change in the stress values is observed along z-axis in figure 29d. Higher temperature gradients exist in the building direction, represented in figure 29c, rather than in horizontal plane, which results in the highest residual stress peaks in the building direction, as observed in figures 28c and 29c when comparing the stress peak values within figures 28 and 29 (Li et al. 2017, p. 165; Liu et al. 2016, p. 651-652). Figure 30 represents the predicted and measured cantilever deformation magnitudes in the building direction along the length of the part (Li et al. 2017, p. 167).
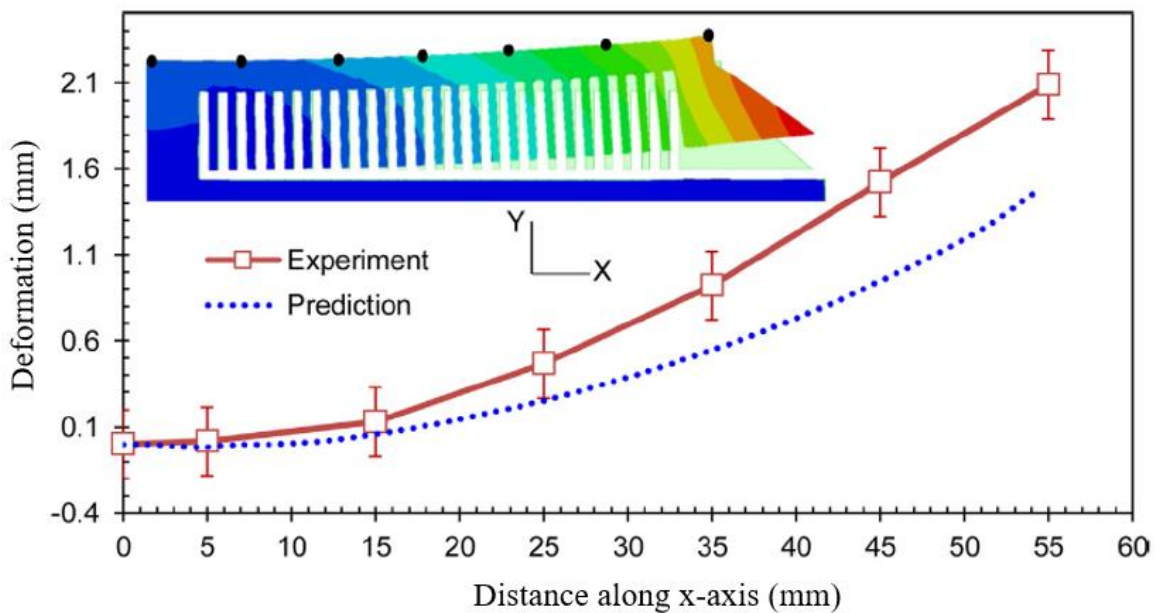

Figure 30. Predicted and measured cantilever deformation magnitudes in the building direction and along x-axis. Laser power of 195 W and scanning speed of 800 mm/s were used. Other parameters are same as in table 4. (Modified from Li et al. 2017, p. 167.)

The black dots in the upper surface of the cantilever arm indicate the measuring points of deformations in figure 30. It can be seen in figure 30 that the prediction and the actual

measurement show similar deformation along the x-axis. Maximum measured deformation in the end of the cantilever is a bit higher (c. 2.1 mm) compared to the predicted one (c. 1.5 mm). (Li et al. 2017, p. 167.) The ends of the cantilever have bent upwards (2.1 mm) almost the measure of thickness of the cantilever arm (3.0 mm).

Scanning strategy has an impact on the formation of residual stresses and deformations in metal parts manufactured by L-PBF as the effect of heat can be controlled by adjusting the scanning strategy (Mercelis & Kruth 2006, p. 264). Li et al. (2015) studied the effect of scanning pattern on the vulnerability of the part to have residual stress and deformations in L-PBF of iron based powder, by modeling a prediction. Li et al. (2015, p. 707-708) examined four scanning patterns in a single layer (35 mm × 15 mm × 0.15 mm) experiment, coated on a 45 mm × 22 mm × 1 mm steel platform. The four scanning patterns of the study are represented in figure 31 (Li et al. 2015, p. 709).
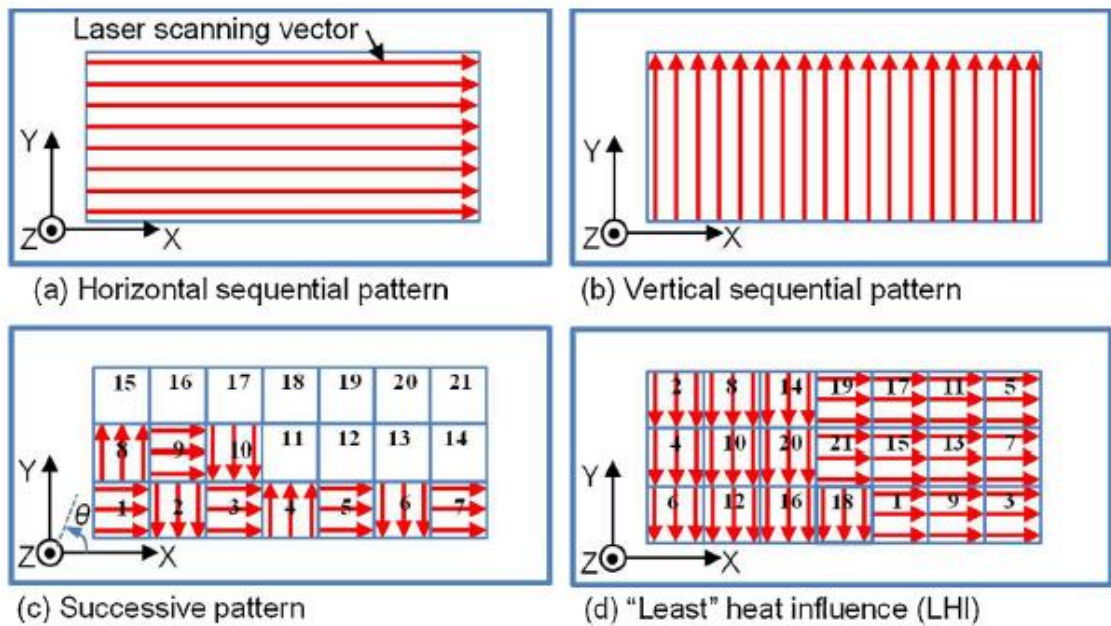

Figure 31. Top view of the four scanning patterns used in the study of Li et al. (2015, p. 709).

Top view of the powder layer is represented in figure 31 for each scanning strategy. The traditional unidirectional scanning strategies are horizontal (in figure 31a) and vertical (in figure 31b) while more advanced strategies are successive pattern (in figure 31c) and least heat influence (in figure 31d). In the successive pattern and least heat influence pattern the

powder layer is divided in sections of 5 × 5 mm rectangles, known as islands, and the numbers in these islands (shown in figure 31) represent their scanning order. (Li et al. 2015, p. 707.) Main parameters used in the model are represented in table 5.

Table 5. Parameters used in the study of Li et al. (2015, p. 706).

Laser power	300 W
Scanning speed	50 mm/s
Focal point diameter	600 µm
Layer thickness	150 µm

Results of the study of Li et al. (2015) comprise the deformations in the building direction along x- and y-axis (length and width of the part, respectively) and residual stresses created along the length of the part. Results are illustrated in figures 32-35. Figure 32 represents the deformation of the part along x-axis (Li et al. 2015, p. 709).
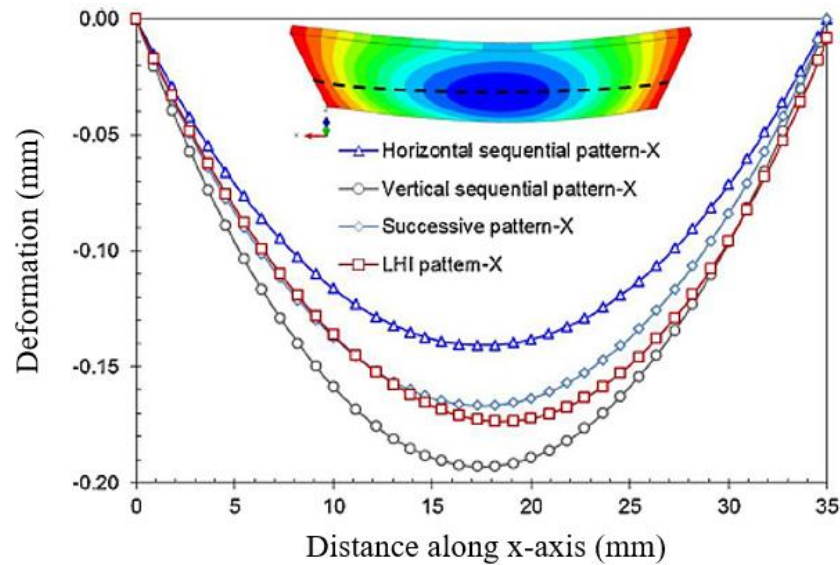

Figure 32. Deformation of the part in building direction along x-axis for four different scanning patterns. Laser power of 300 W and scanning speed of 50 mm/s were used. Other parameters are same as in table 5. (Modified from Li et al. 2015, p. 709.)

It can be seen in figure 32 that the middle section of the part has bent downwards (or the ends have bent upwards), which follows the TGM and cool-down mechanism. Horizontal sequential pattern results in the smallest deformations (c. 0.14 mm) and vertical sequential

pattern results in largest deformations (c. 0.19 mm) along the length of the part. The other two scanning strategies that utilize the island strategy, result in almost equal deformations to each other and set in middle between the horizontal and vertical patterns, which was also found in the study of Kruth et al. (2004, p. 618-619). (Li et al. 2015, p. 710.) Figure 33 represents the deformation along y-axis (Li et al. 2015, p. 710).
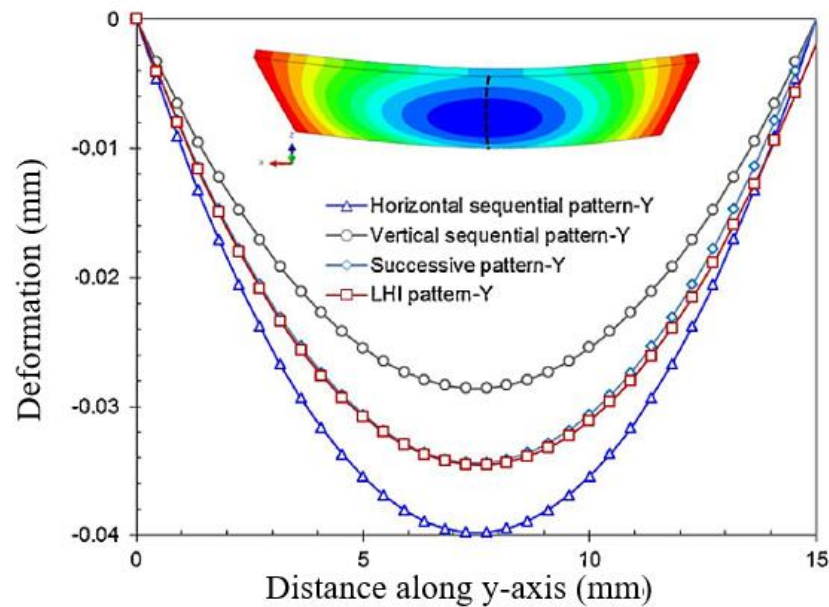

Figure 33. Deformation of the part in building direction along y-axis for four different scanning patterns. Laser power of 300 W and scanning speed of 50 mm/s were used. Other parameters are same as in table 5. (Modified from Li et al. 2015, p. 710.)

It can be seen in figure 33 that the same behavior that was obtained in figure 32, can be obtained here also but the phenomenon is vice versa. Largest deformation (c. 0.04 mm) is observed with horizontal sequential pattern whereas the smallest deformation (c. 0.029 mm) is observed with vertical sequential pattern along the width of the part. The other two scanning strategies again share equal deformations and set in the middle between the horizontal and vertical patterns. (Li et al. 2015, p. 710.) Similar behavior was also found in the study of Kruth et al. (2004, p. 619). Based on the results shown in figures 32 and 33, it can be observed that the smallest deformations are created in the part along scanning vector and the largest deformations perpendicular to the scanning vector (Kruth et al. 2004, p. 618-619; Li et al. 2015, p. 710). Figure 34 represents the residual stresses generated in the part along its length (Li et al. 2015, p. 711).
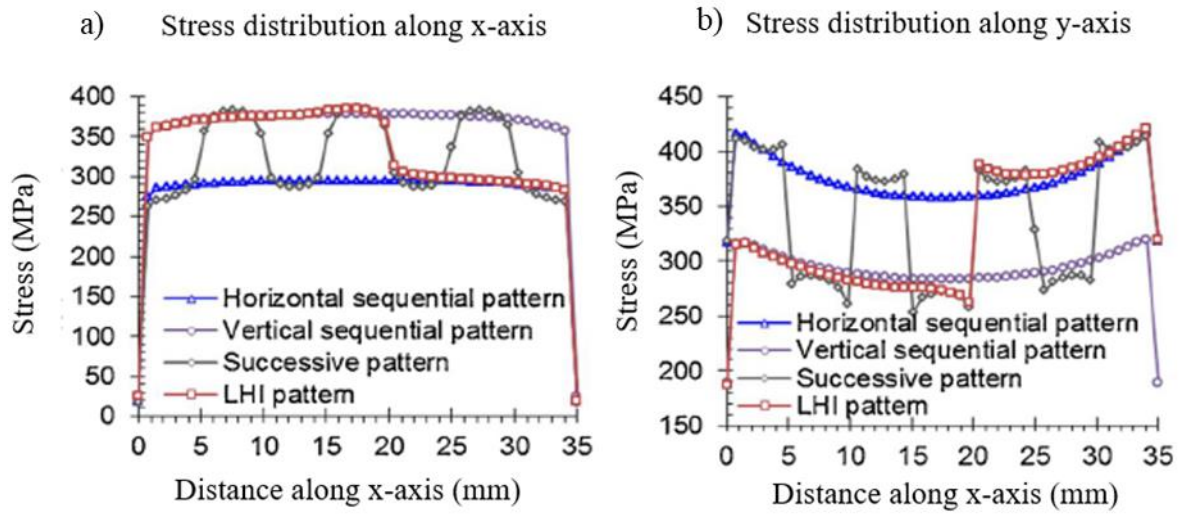
Figure 34. Residual stresses in (a) x- and (b) y-axis along the length of the part for four different scanning patterns, stresses measured on top surface. Laser power of 300 W and scanning speed of 50 mm/s were used. Other parameters are same as in table 5. (Modified from Li et al. 2015, p. 711.)

It can be seen in figure 34 that the residual stresses mirror to the deformations obtained in figures 32 and 33 as the largest deformation is observed with the highest residual stress and vice versa (see for example vertical sequential pattern deformation along x-axis in figure 32 and its residual stress along x-axis in figure 34a). Unidirectional horizontal and vertical patterns create quite stable residual stress graphs whereas the advanced successive pattern and least heat influence pattern create oscillating residual stresses because the scanning vector changes its direction multiple times during the process. (Li et al. 2015, p. 711.) Similar behavior was also found in the study of Mercelis & Kruth (2006, p. 260-261). Successive pattern and least heat influence scanning strategies seem to make a compromise between the horizontal and vertical patterns when it comes to deformations in the part, creating moderate deformations rather than large ones in certain direction. Horizontal and vertical patterns perform the best in generating the smallest residual stresses and deformations in only one direction but then again, the perpendicular direction to that will have the largest residual stresses and deformations. (Li et al. 2015, p. 709-711.)

However, Liu et al. (2016) and Li et al. (2018) found deviant results to the studies of Mercelis & Kruth (2006) and Li et al. (2015) relating to the residual stresses in the part. Liu et al. (2016, p. 652-653) and Li et al. (2018, p. 31, 35) found that residual stress is at its highest

along scanning vector and its lowest perpendicular to the scanning vector, which is opposite result to the studies of Mercelis & Kruth (2006, p. 260-261) and Li et al. (2015, p. 711). Figure 35 represents the results of the study of Liu et al. (2016, p. 653) concerning the residual stresses along scanning vector (x-axis) and perpendicular to the scanning vector (z-axis). The effect of scanning length on the residual stress can also be seen in figure 35 (Liu et al. 2016, p. 653).
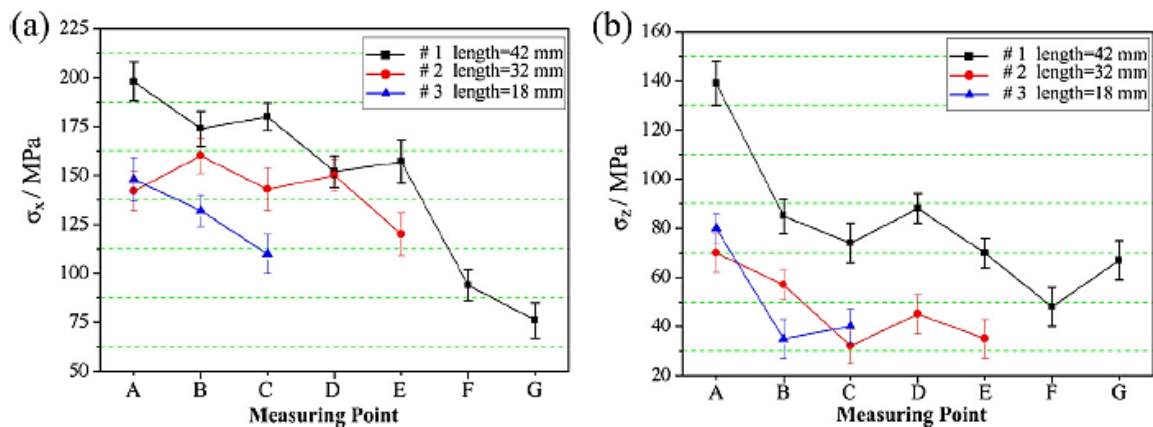

Figure 35. Planar residual stresses along (a) x- (longitudinal) and (b) z-axis (transverse) generated with three different scanning lengths in a rectangular geometry. Measuring points are distributed equally along the scanning lengths. Laser power of 200 W and scanning speed of 400 mm/s were used. (Liu et al. 2016, p. 653.)

It can be seen in figure 35a that the stress along scanning direction is higher compared to the stress along perpendicular direction in figure 35b, with all the scanning lengths examined, which is the opposite result to the studies of Li et al. (2015, p. 711) and Mercelis & Kruth (2006, p. 260-261) (Li et al. 2018, p. 35; Liu et al. 2016, p. 653). It can also be observed in figure 35 that the longest scanning vector results in the highest stress values and the shortest scanning vector results in the lowest stress values (Liu et al. 2016, p. 653; Mercelis & Kruth 2006, p. 264). This occurs because longer tracks contract more than shorter ones and when the contraction is limited, it results in higher residual stress for the longer tracks (Liu et al. 2016, p. 653). However, Liu et al. (2016, p. 650-651) share similar results with Mercelis & Kruth (2006, p. 256-257) about the matter that the tensile residual stresses are generated on the surface of the part whereas compressive stresses locate inside the part. Also, Liu et al. (2016, p. 651-652) agree with Li et al. (2017, p. 165) that the highest stress values are

observed in the building direction rather than in horizontal plane. Also the highest deformations occur in the building direction according to Wu et al. (2014, p. 6264).

Overall, there will always be a level of residual stress in parts after build despite the scanning strategy used. Despite the scanning strategy, the highest residual stresses are generated in the building direction rather than in horizontal plane (Li et al. 2017, p. 165; Liu et al. 2016, p. 651-652). Also larger deformations occur in the building direction than horizontally (Wu et al. 2014, p. 6264). The deformation shape obeys the TGM and cool-down mechanism that pursue to lift the edges of parts from the building platform. Therefore, parts that are built in different orientations, have different deformation shapes. (Wu et al. 2014, p. 6264.) Parts can be complex by shape and different scanning strategies may be required to be used. Parts can be built with scanning patterns that are varied for each layer in order to compensate the effect of heat and generation of residual stresses and deformations in the part. For example, scanning pattern can be rotated for each new layer to achieve regular variation in the scanning direction. (Renishaw 2017.)

3   AIM AND PURPOSE OF EXPERIMENTAL PART

L-PBF of metal materials is gaining interest in the manufacturing industry (Wohlers et al. 2018, p. 161). Due to limitations of L-PBF comprising the residual stresses and possible deformations in parts, which may prevent them to be used in their function, the technology needs more research.

Motivation for this thesis was to study the deformation behavior of metal parts in L-PBF. An experimental part was performed in addition to the literature review. Experimental part was implemented by designing simple shapes with CAD software, manufacturing them by L-PBF and capturing their deformations with a macroscope. Aim of the experimental part was to notice the deformation shape by examining different geometries built in different orientations. Based on the results to be observed in the experiments, conclusions of deformation behavior can be done with the observations made in the literature review.

Two different test sets were done in the experiments in order to study the effect of geometry and building direction of the part on the formation of deformations. Rectangular shapes were built in different orientations in test set 1 to see which shapes and orientations cause deformations and which kind of deformation. Accumulation of heat in the building direction was pursued in test set 2 with geometries that have different thickness along the building direction to see the impact of accumulation of heat.

Purpose of the experimental part was to demonstrate the challenges of L-PBF utilizing metal material when it comes to deformations of parts and to find ways to prevent these problems. These results can be industrially implemented in practical cases.

4   EXPERIMENTAL SETUP

Experimental setup of this thesis is represented in this chapter. Test samples were modeled with SolidWorks 2018 CAD software and the test samples were manufactured by EOS Finland Oy, in Turku, with EOS M 290 L-PBF machine. Deformations were analyzed with Keyence VR-3200 macroscope at LUT University in Lappeenranta. The test samples used in the experiments were designed and manufactured only for studying the deformations of SS 316L parts and they do not serve any other purpose.

4.1 Material

The test samples were manufactured of EOS StainlessSteel 316L powder of which material composition is represented in table 6 and material properties of parts made of the material are represented in table 7 (EOS 2017, p. 2-3).

Table 6. Material composition of EOS StainlessSteel 316L powder (EOS 2017, p. 2).

Element	Content (weight-%)	
	Min.	Max.
Cr	17.00	19.00
Ni	13.00	15.00
Mo	2.25	3.00
C		0.030
Mn		2.00
Cu		0.50
P		0.025
S		0.010
Si		0.75
N		0.10

Table 7. Material properties of parts made of EOS StainlessSteel 316L (EOS 2017, p. 3).

Density	7.9 g/cm^3
Ultimate tensile strength	590 MPa
Yield strength	500 MPa
Elongation at break	46.7 %

The tensile test values represented in table 7 are determined in parts made with vertical and horizontal orientations and the numbers are average values of them. Tensile test values are determined according to ISO 6892 / ASTM E8M. (EOS 2017, p. 3.)

4.2 Equipment

The test samples were manufactured by EOS Finland Oy in Turku and deformations were analyzed with a macroscope at LUT University in Lappeenranta.

4.2.1 Equipment for L-PBF

The test samples were manufactured by EOS M 290 machine, represented in figure 36, with specifications and parameters shown in table 8 (EOS 2019).

Figure 36. EOS M 290 L-PBF machine (EOS 2019).

Table 8. Specifications and parameters used in the experiments.

Machine	EOS M 290
Parameter set	316L 40µm FlexLine
Build area	250 mm × 250 mm × 325 mm
Layer thickness	40 µm
Shielding gas	Argon
Focal point diameter	70-80 µm
Platform temperature	80 ˚C
Average particle size distribution	20-53 µm

As seen in table 8, parameter set 316L 40µm FlexLine was used to build the test samples. For all tests, standard parameters for SS 316L were used.

4.2.2 Equipment for macroscopic analysis

Equipment used to capture the deformations in the test samples was Keyence VR-3200 macroscope which is represented in figure 37.
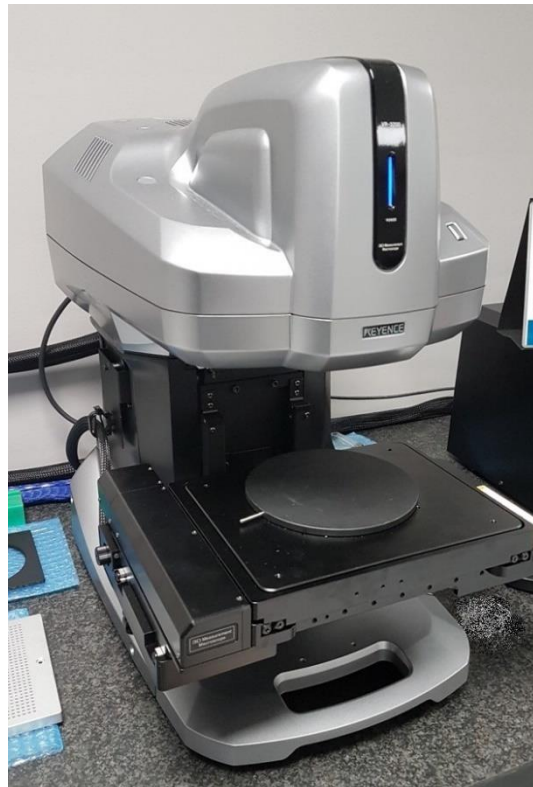
Figure 37. Keyence VR-3200 macroscope.

The macroscope represented in figure 37 has maximum measuring volume of 184 mm × 88 mm × 90 mm and planar measurement accuracy of ±5 µm in wide-field mode that was used in the experiments. The wide-field mode allows to take maximum of 24.0 mm × 18.0 mm image and with a stitching function, the whole measuring area can be captured.

4.3 Test samples

Different geometries were designed in order to examine the deformations. Two sets of test samples were designed: test set 1 and test set 2. In test set 1, the first design was a cube, which was further edited into square and rectangular shapes and positioned in different orientations (horizontal, vertical and in 45˚ angle) on the building platform. Purpose of test set 1 was to examine which geometries and orientations cause deformations and which kind of deformation. The test samples have differences in layer number and scanning areas which result in different magnitudes of thermal stresses. Table 9 represents the test samples of the test set 1.

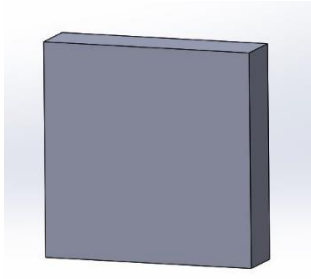*Table 9. Test samples of test set 1.*
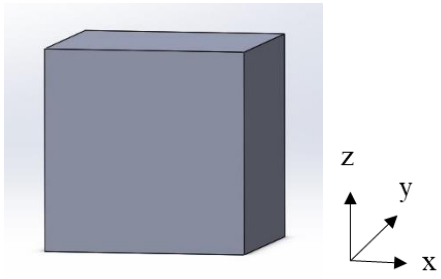
Test sample and dimensions	Orientation (building direction along z-axis)
A1 (20 mm × 20 mm × 20 mm)	
B1 (20 mm × 5 mm × 20 mm)	

Table 9 continues.
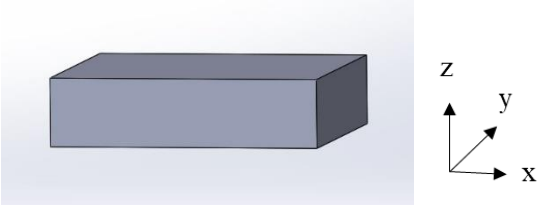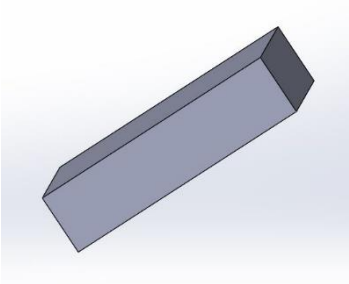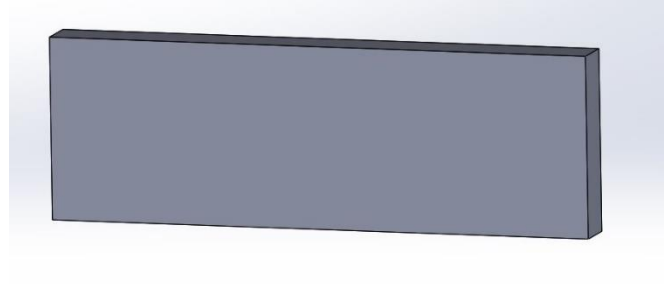
Test sample and dimensions	Orientation (building direction along z-axis)
B2	
B3	
C1 (60 mm × 5 mm × 20 mm)	
C2	

Table 9 continues.
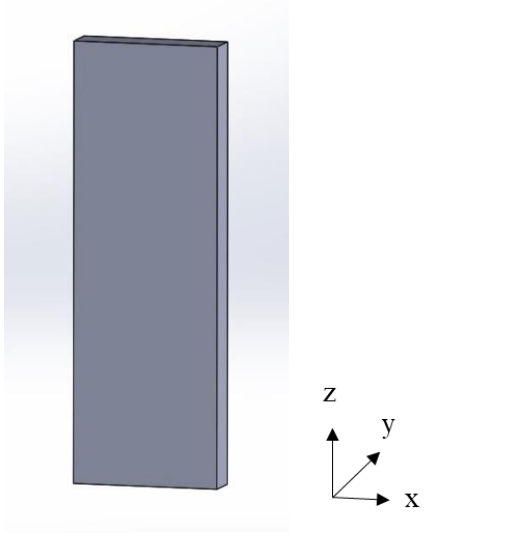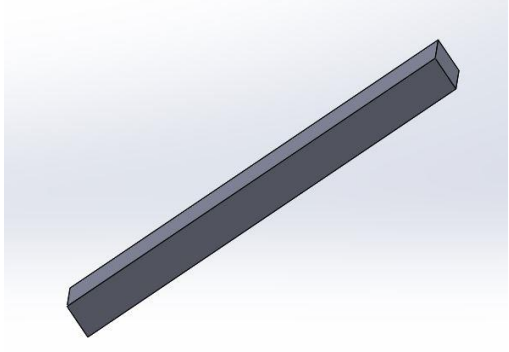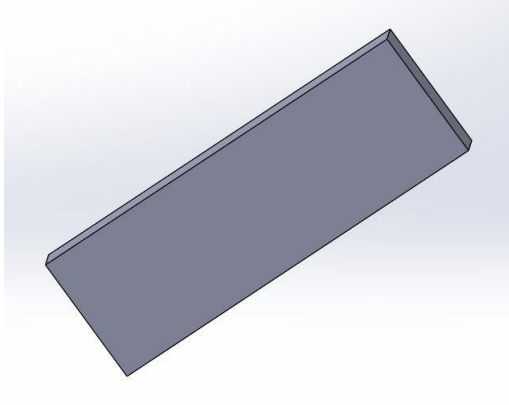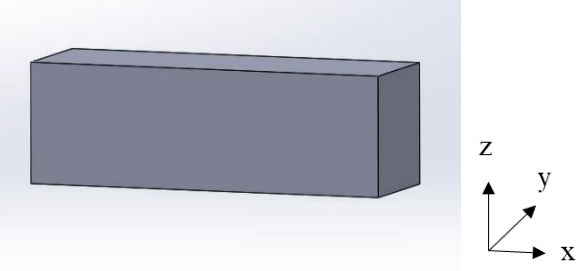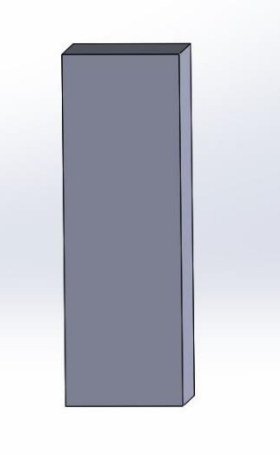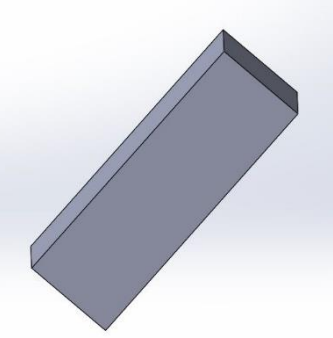
Test sample and dimensions	Orientation (building direction along z-axis)
C3	
C4	
C5	

Table 9 continues.

Test sample and dimensions	Orientation (building direction along z-axis)
D1 (60 mm × 20 mm × 20 mm)	
D2	
D3	

Letter in the test sample name in table 9 indicates the geometry of the test sample and the number indicates orientation of the specific test sample on the building platform, meaning that all the test samples with same letter are dimensionally equal. Test sample A is a cube and test samples B1, B2 and B3 are squares in different orientations on the building platform. Test samples C1, C2, C3, C4 and C5 are rectangular shapes in different orientations and test samples D1, D2 and D3 are square bars in different orientations.

Excessive local accumulation of heat is not expected to occur in any of the test samples in test set 1 because the geometries are uniform. On the other hand, the test samples have large areas to be scanned which induces high heat input. This creates high thermal stresses that can cause deformations. Figure 38 represents a schematic of heat transfer within test sample D1 as demonstration.
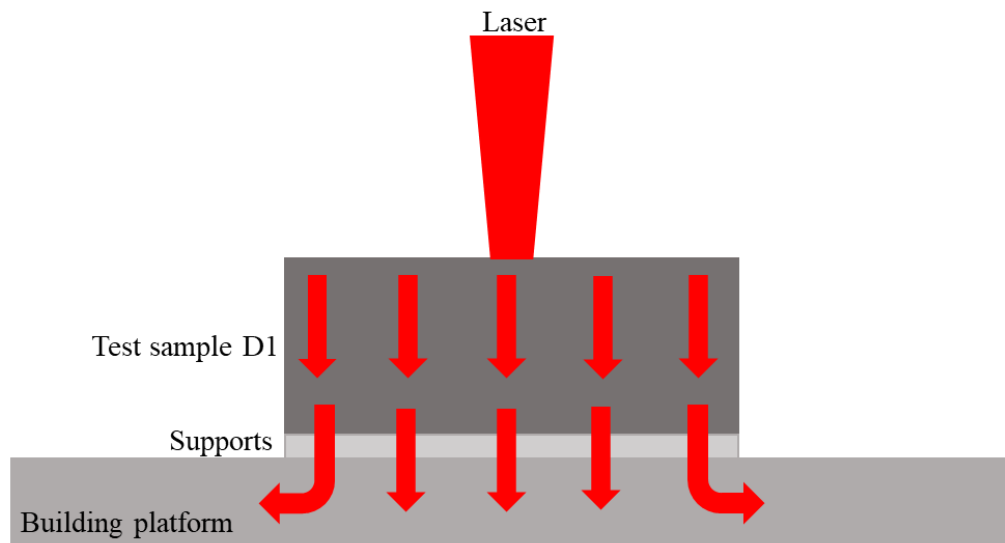

Figure 38. Schematic of heat transfer within test sample D1.

As figure 38 demonstrates, the heat transfers through the part during the build without accumulating into certain areas. The scanning volume is large as the test sample is a solid block and not optimized by any means. The heat transfer is more or less similar in all of the test samples in test set 1. Especially the rectangular shapes that are orientated horizontally (C1, C2 and D1) are vulnerable to have some deformation due to the TGM and cool-down mechanism, as observed in the studies of Li et al. (2015, p. 709), Li et al. (2017, p. 165-167) and Wu et al. (2014, p. 6264).

Test set 2 includes test samples with more varying geometries along the building direction whereas test set 1 has uniform geometries. The test samples of test set 2 are represented in table 10.

Table 10. Test samples of test set 2.
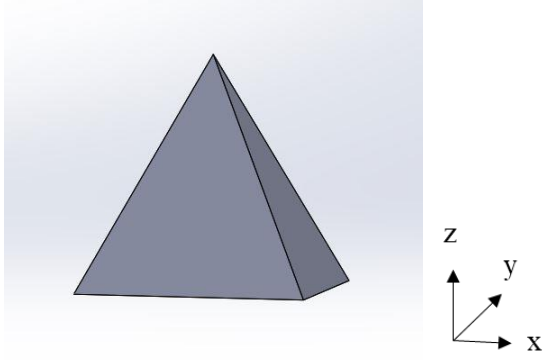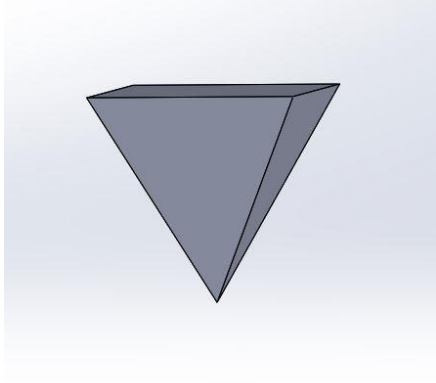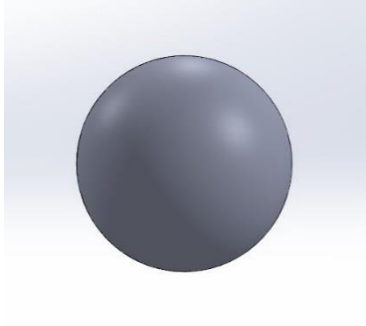
Test sample and dimensions	Orientation (building direction along z-axis)
E1 (30 mm × 30 mm × 30 mm)	
E2	
F (ø 20 mm)	

Table 10 continues.
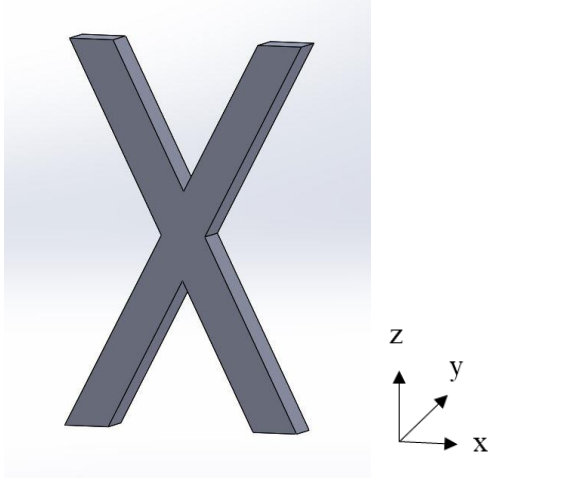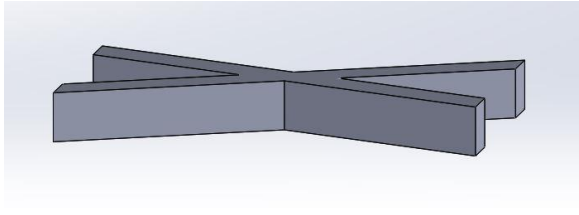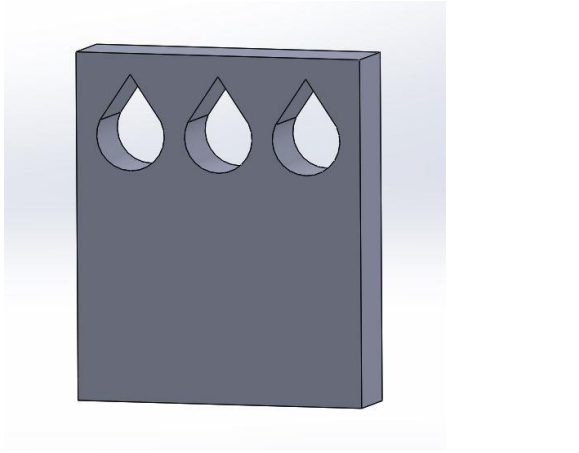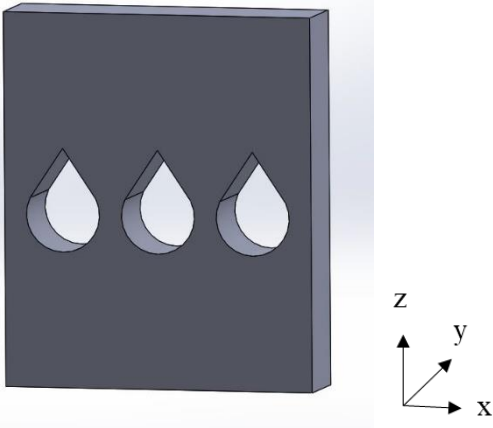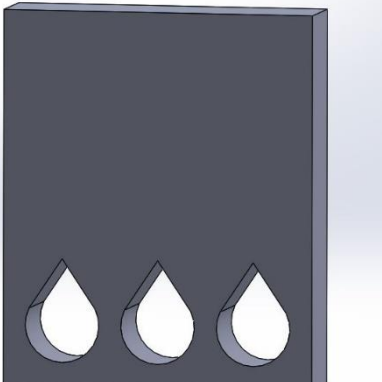
Test sample and dimensions	Orientation (building direction along z-axis)
G1 (40 mm × 7.5 mm × 65 mm)	
G2	
H (42 mm × 10 mm × 50 mm)	

Table 10 continues.

Test sample and dimensions	Orientation (building direction along z-axis)
I (42 mm × 10 mm × 50 mm)	
J (42 mm × 10 mm × 50 mm)	

Test samples in table 10 are named with the same principle used in naming the test samples of test set 1. Test samples E1 and E2 are pyramid shapes with two different orientations, test sample F is ball, test samples G1 and G2 are crosses with two different orientations and test samples H, I and J are blocks that have three penetrating holes in different locations of the block. The holes are droplet shaped in order to avoid using support structures inside them.

The accumulation of heat especially in the building direction was pursued in test set 2. The heat will accumulate in the part as all the heat transfers through its height towards the building platform (Yang et al. 2017, p. 608; Yang & Wang 2008, p. 1065). Excessive increase in part temperature may cause a failure during the build because of high thermal stresses and lowered yield strength of the material (Kruth et al. 2004, p. 617). Figure 39 represents a demonstration of the accumulation of heat.
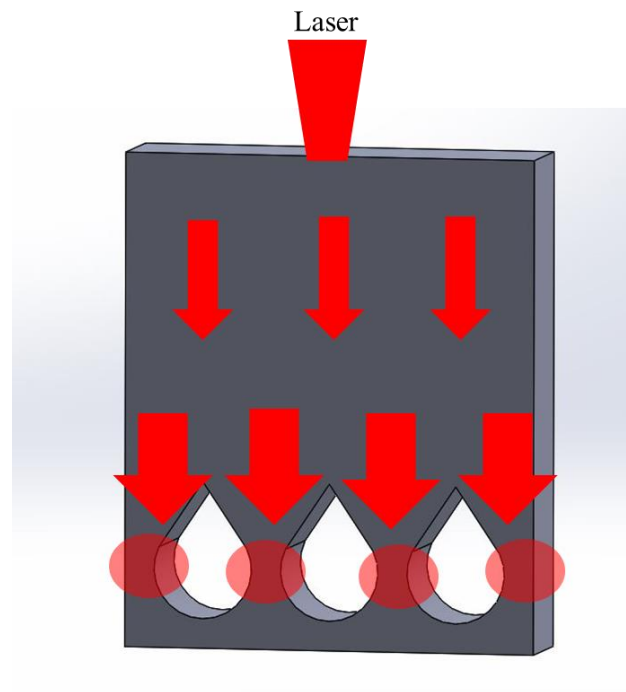
Figure 39. Schematic of accumulation of heat in test sample J.

As figure 39 demonstrates, the heat that is input while building the upper solid part of test sample J, transfers through the thin walls of the bottom region of the test sample (circled in red). These thin walls may suffer from defects as the heat may accumulate into these narrow sections that are not capable of transferring the heat as effectively as the larger solid area above them.

5   EXPERIMENTAL PROCEDURE

All the test samples were manufactured and they were removed from the building platform as built, with no post-processing performed. The effect of machine parameters (such as laser power, scanning speed, focal point size, hatch spacing, scanning strategy, scan length, layer thickness), powder properties (such as packing efficiency and particle size) and support structure parameters, were neglected, as they all were constant during the experiments. This leaves the geometry and vertical orientation of the part to be the variable parameters.

5.1 Manufacturing of test samples with L-PBF

The first stage of the experimental procedures in this thesis was to design the test samples. 3D-models of the test samples were made with SolidWorks 2018 CAD software and the files were converted into suitable file form (.stl) for the AM machine. The orientation of the test samples on the building platform was chosen individually for each test sample and the required support structures for each test sample were added to the models. Yet the models were sliced in order to be readable for the AM machine. After these procedures the models were ready for printing. Figure 40 represents the building platform on which the test samples are positioned for the build.
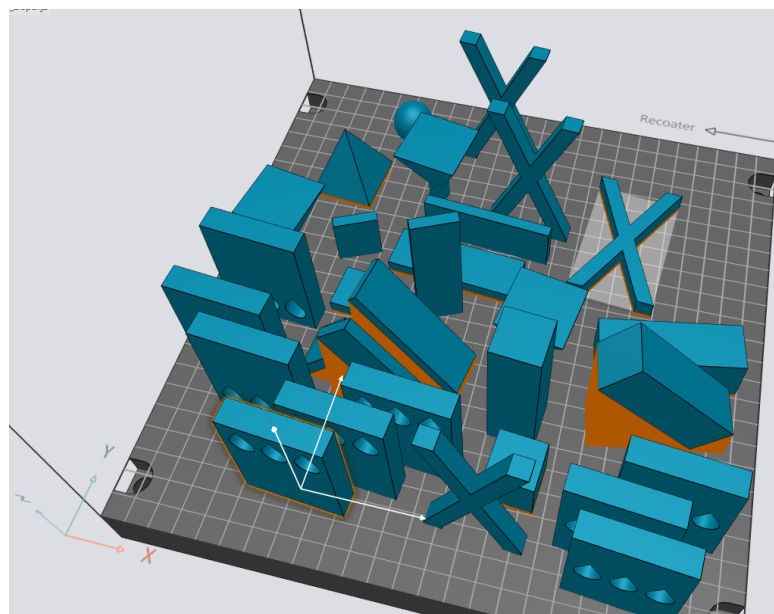

Figure 40. The test samples positioned on the building platform for the build. Support structures are indicated in orange.

All the test samples were manufactured in the same run represented in figure 40. Before starting the build, process parameters were set. The standard parameters for SS 316L were used for all the test samples.

The building platform was removed from the AM machine once the build was completed and excess powder was removed from the test samples. No thermal stress relief was performed in order to examine the test samples as built. The test samples were cut from the building platform and the support structures were removed and since no post-processing operations were performed.

5.2 Analysis of test samples with macroscope

Macrographs of test samples were captured in order to detect possible deformations. As the residual stresses induced by TGM pursue to lift the edges of parts from the building platform and the largest deformations are observed in the building direction, macrographs of each test sample were captured in order to detect the deformation in the building direction (Kruth et al. 2004, p. 617; Simson et al. 2017, p. 185; Wu et al. 2014, p. 6264). Macrographs of test samples were captured one test sample at a time. At first, the test sample was positioned on the macroscope platform. The largest wide-field mode available was used which allows to take image of 24.0 mm × 18.0 mm area at a time. Therefore, macrographs of the test samples longer than 24.0 mm were captured by taking multiple images of 24.0 mm at a time as long as the whole test sample was captured and the images were joined together with a stitching function. The image was focused to the surface of the part with autofocus function. The longest test samples required three images to be taken and joined. When images of a whole test sample were taken, the stitched images were automatically positioned into correct position to form the complete macrograph and a grid was added to each macrograph in order to clarify the deformation magnitude.

6   RESULTS AND DISCUSSION

This chapter represents the results observed in the experimental part in which deformation was studied in test samples made of SS 316L by L-PBF. Results of test set 1 are represented in figures 41-49 and results of test set 2 are represented in figures 50-56. Figure 41 represents the test samples A1, B1, B2 and B3.
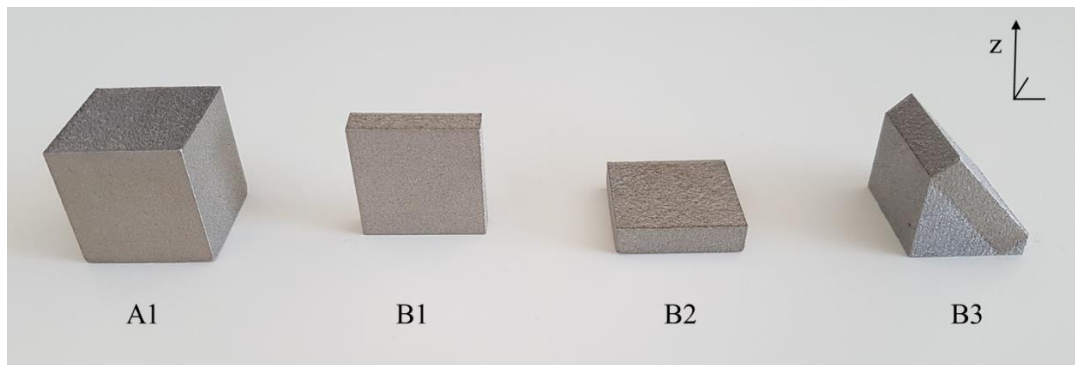
Figure 41. Test samples A1, B1, B2 and B3 (with support structures). Building direction along z-axis.

No evident deformation can be observed in test samples represented in figure 41. Figure 42 shows macrographs of test samples A1, B1, B2 and B3.
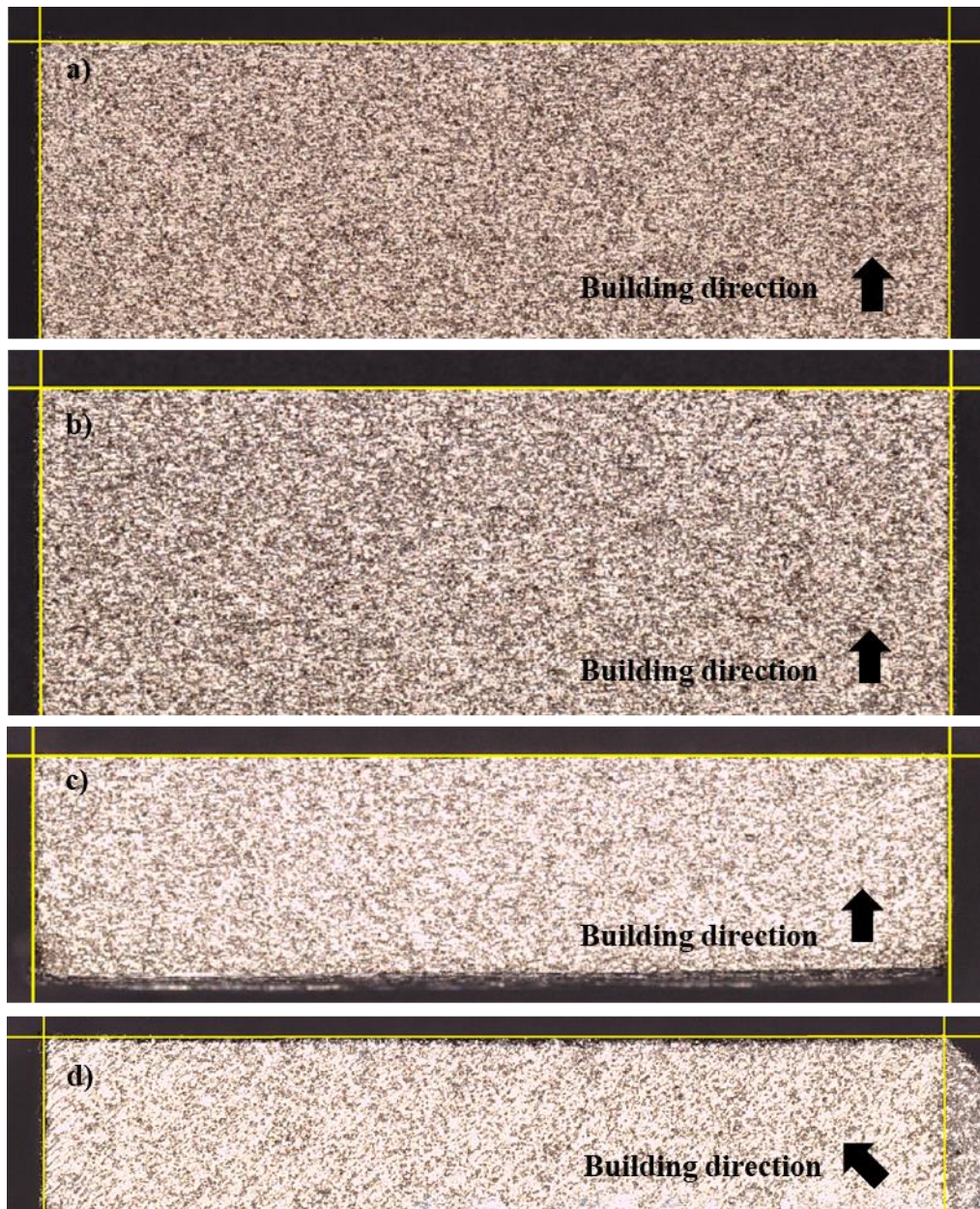
Figure 42. Macrographs of test samples (a) A1, (b) B1, (c) B2 and (d) B3 (support structures removed from bottom surface). Front view, building direction is indicated with arrow.

No deformation can be observed in any of the test samples represented in figure 42. Rough surface can be obtained in test sample B3 (see the top surface in figure 42d) due to stair-step effect that is typical in sloping surfaces (EOS 2018, p. 3).

Test samples C1, C2, C3, C4 and C5 are represented in figure 43.
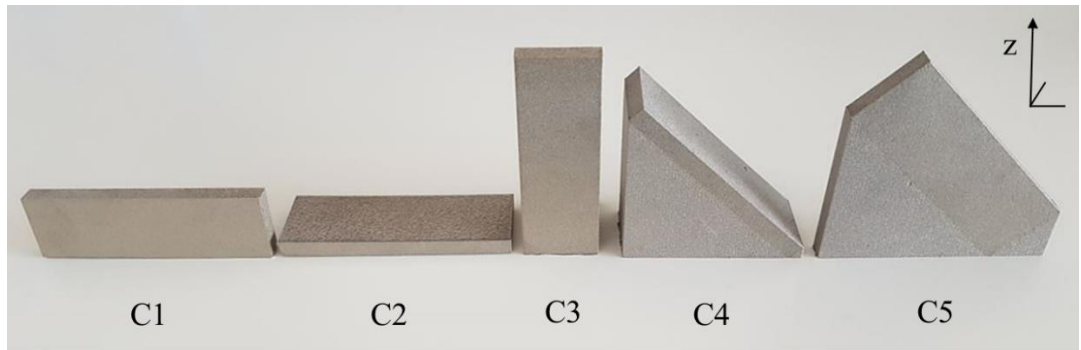
Figure 43. Test samples C1, C2, C3, C4 (with support structures) and C5 (with support structures). Building direction along z-axis.

Test sample C2 is the only one to have evident deformation of test samples represented in figure 43. Figure 44 represents test sample C2.

Figure 44. Test sample C2, building direction along z-axis.

It can be seen in figure 44 that the edges of test sample C2 have bent upwards (indicated with red arrows) which obeys the TGM and cool-down mechanism (see in figures 14 and 15).

Macrographs of test samples C1, C2, C3, C4 and C5 are represented in figure 45.
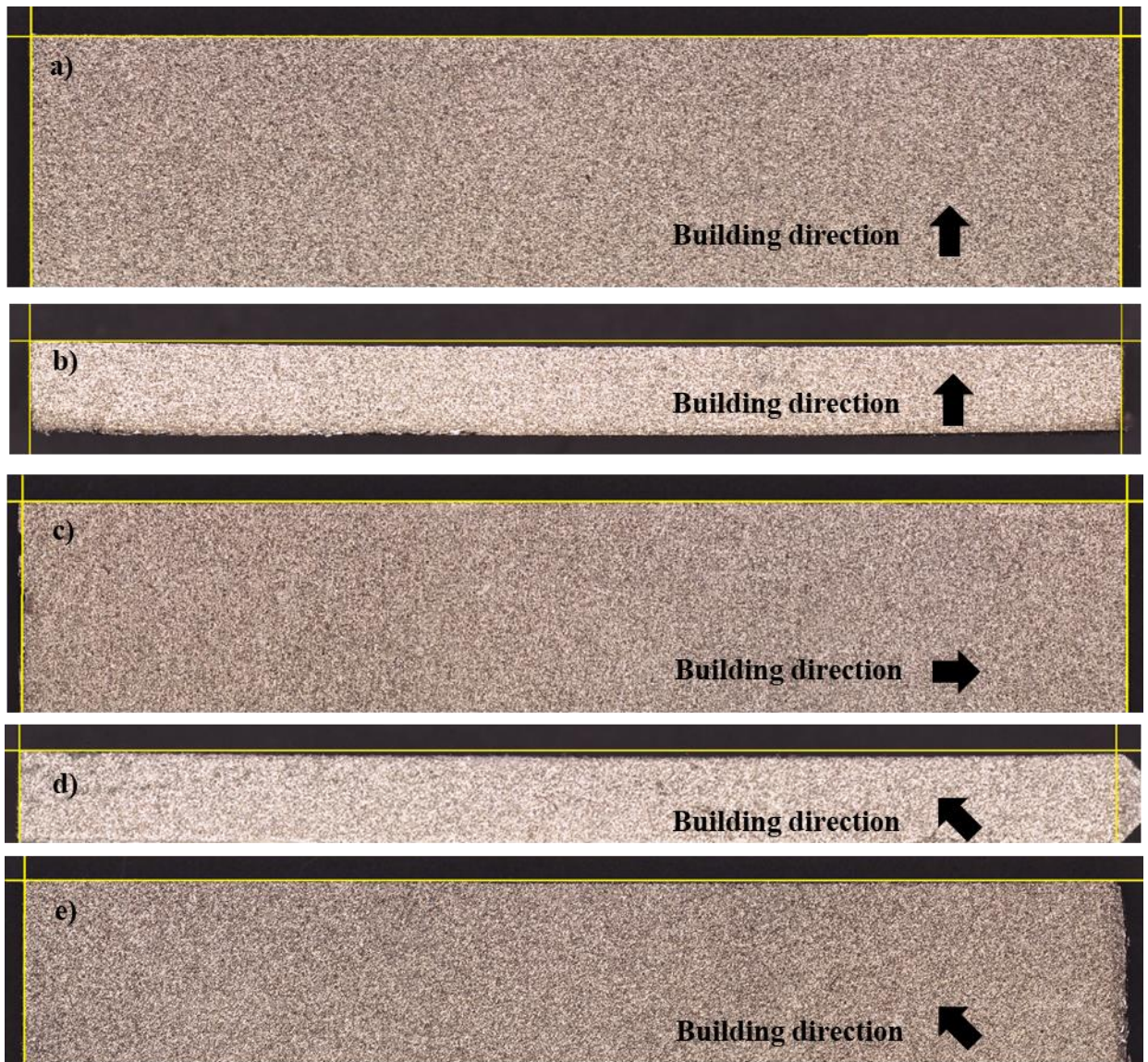
Figure 45. Macrographs of test samples (a) C1, (b) C2, (c) C3, (d) C4 and (e) C5 (support structures removed from C4 and C5). Front view, building direction is indicated with arrow.

Test samples C1, C2, C3, C4 and C5 are dimensionally equal and only their building orientation was varied. However, test samples C2 and C4 have deformations, as it can be seen in figures 45b and 45d. The deformation shapes of test samples C2 and C4 are similar and they obey the TGM and cool-down mechanism. It can be noticed from figure 43 that test samples C1 and C2 were both built horizontally but only C2 has deformation, as it can be observed in figures 45a and 45b. Test sample C2 was orientated flat whereas test sample C1 was orientated on its side (see figure 43). Test sample C1 is higher and stiffer in the building direction to resist the deformation compared to test sample C2. This is illustrated in figure 46.
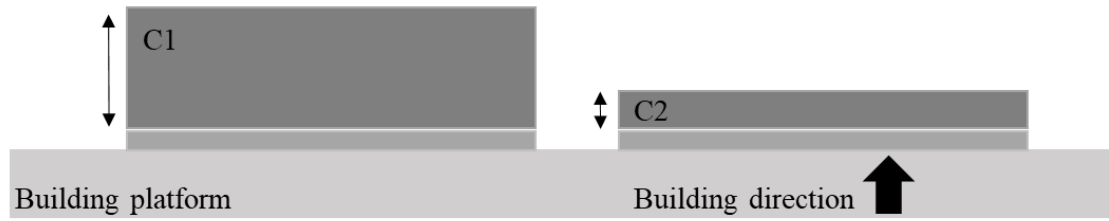
Figure 46. Schematic of test samples C1 and C2 on the building platform.

Test sample C1 has more material in the building direction and more stiffness, as observed in figure 46. Also the scanning area of a single layer is smaller in test sample C1. Smaller scanning area contracts less than larger one (Liu et al. 2016, p. 653). This same result and conclusion can be observed between test samples C4 and C5 represented in figures 45d and 45e of which both were built in 45˚ angle and only C4 has deformation. C4 was orientated flat and C5 on its side (see figure 43). The deformation of test sample C4 occurred after the support structures were removed from the part as no deformation was observed while the support structures were still attached to the part. Figure 47 represents a macrograph of test sample C4 with support structures still attached. Also macrograph of the test sample without support structures is represented in figure 47 for comparison.

Figure 47. Macrographs of test sample C4 (a) with support structures and (b) without support structures. Front view, building direction is indicated with arrow.

As it can be seen in figure 47a, no deformation can be observed in test sample C4 with support structures still attached while evident deformation can be seen in figure 47b. It is typical that the residual stresses are released during the support structure removal (Li et al. 2017, p. 165; Mercelis & Kruth 2006, p. 263-264).

Test samples D1, D2 and D3 are represented in figure 48.
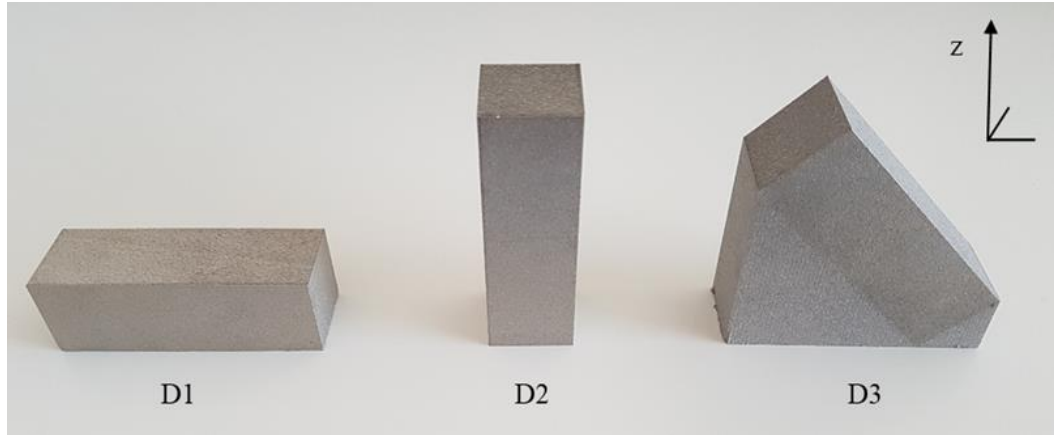
Figure 48. Test samples D1, D2 and D3 (with support structures). Building direction along z-axis.

Test samples D1, D2 and D3 do not show any evident deformation in figure 48.

Macrographs of test samples D1, D2 and D3 are shown in figure 49.

Figure 49. Macrographs of test samples (a) D1, (b) D2 and (c) D3 (support structures removed from bottom surface). Front view, building direction is indicated with arrow.

No deformations can be observed in the macrographs represented in figure 49.

The results of test set 2 are represented in figures 50-56. Test samples E1, E2, F, G1 and G2 are represented in figure 50.
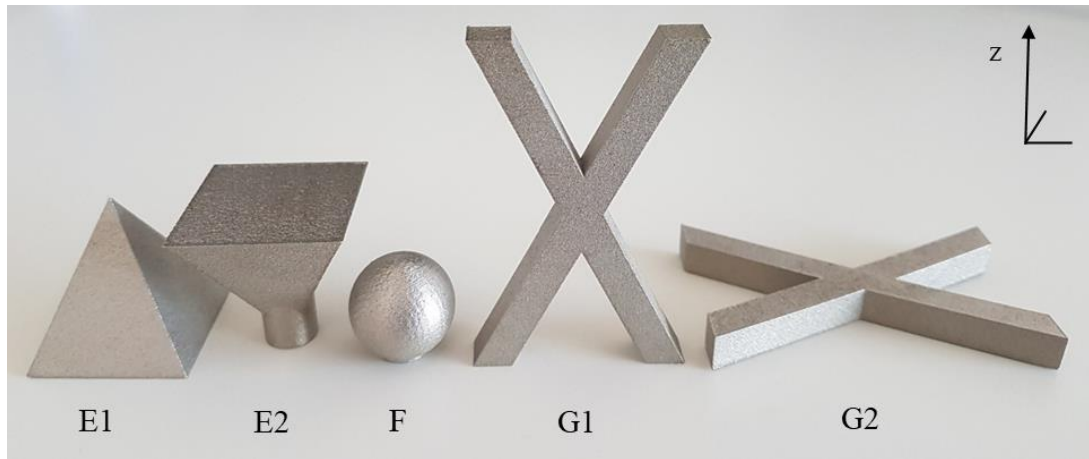
Figure 50. Test samples E1, E2 (with support structures), F (with support structures), G1 and G2. Building direction along z-axis.

Macrographs of test samples E1 and F were not captured due to the challenges of getting images reliable enough to evaluate the test sample shape. However, no evident deformation could be observed in them nor in test samples E2 or G1 represented in figure 50. Test sample G2 shows evident deformation, which can be seen in figure 51.
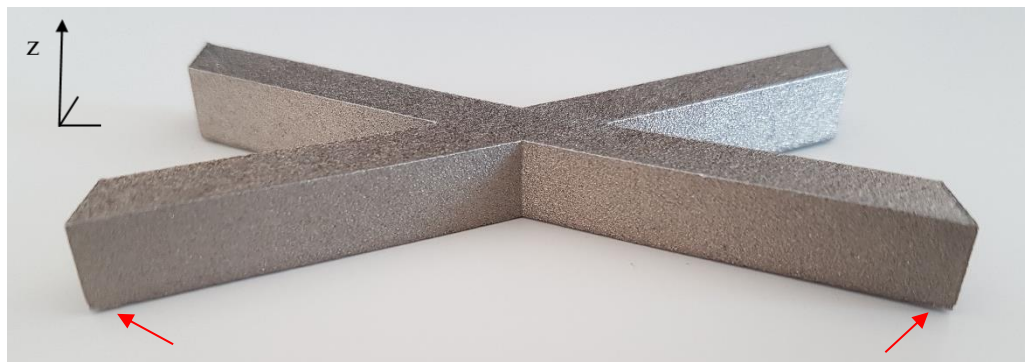
Figure 51. Test sample G2, building direction along z-axis.

It can be seen in figure 51 that the edges of test sample G2 have bent upwards (indicated with red arrows) similarly to test sample C2 (see figure 44). This deformation shape is result

of the TGM and cool-down mechanism that lift the edges of parts from the building platform (see in figures 14 and 15).

Macrographs of test samples G1 and G2 are represented in figure 52. The same side is captured in both test samples for comparison.
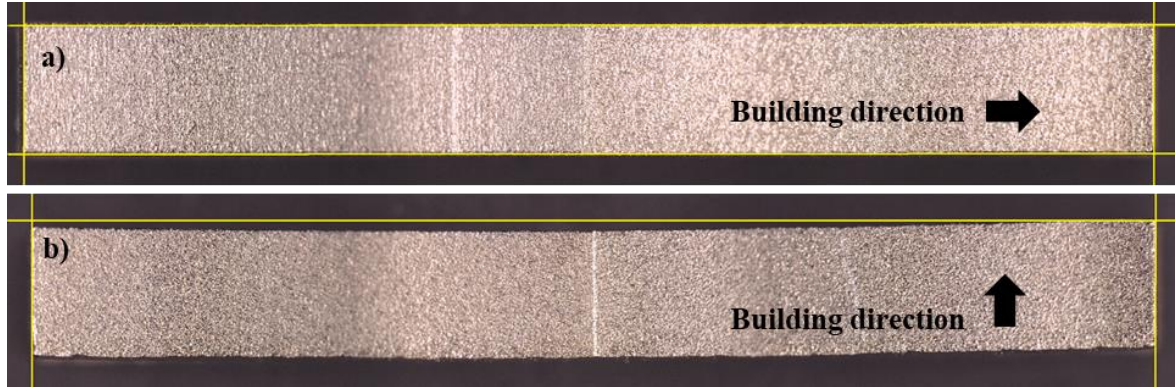
Figure 52. Macrographs of test samples (a) G1 and (b) G2 (building direction is indicated with arrow).

Deformation of the top surface of test sample G2 can be observed in figure 52b. Similar deformation occurred in test samples C2 and C4 (see figures 45b and 45d). Again, test samples G1 and G2 are dimensionally equal but G2 has deformation while G1 does not. G1 was built vertically and G2 horizontally flat (see figure 50). In addition to test samples C2 and G2, test samples B2, C1 and D1 (represented in figures 41, 43 and 48) were built horizontally but without deformation. Test samples C1 and D1 are higher and stiffer in the building direction to resist the deformation. Test sample B2 is much shorter compared to C2 or G2 which makes it more difficult to capture the deformation as smaller area contracts less (Liu et al. 2016, p. 653). Figure 53 illustrates the difference of test samples B2 and C2.
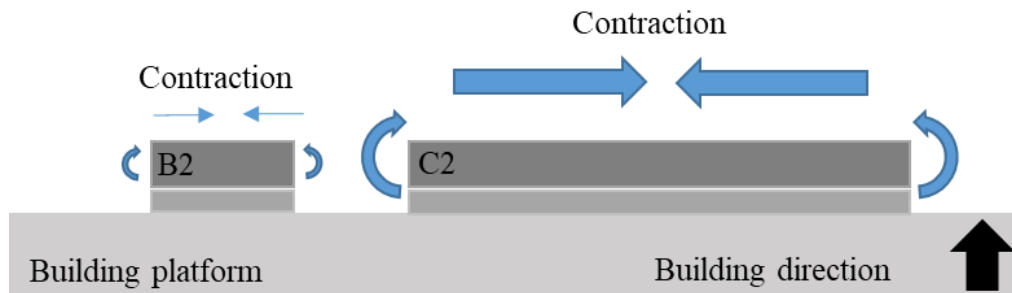
Figure 53. Schematic of test samples B2 and C2 on the building platform.

The larger arrows in touch with test sample C2 in figure 53 indicate that the test sample C2 contracts more than test sample B2.

Macrograph of test sample E2 is represented in figure 54.

Figure 54. Macrograph of test sample E2. Front view, building direction is indicated with arrow.

No deformation can be observed in test sample E2 in figure 54.

Test samples H, I and J are represented in figure 55.
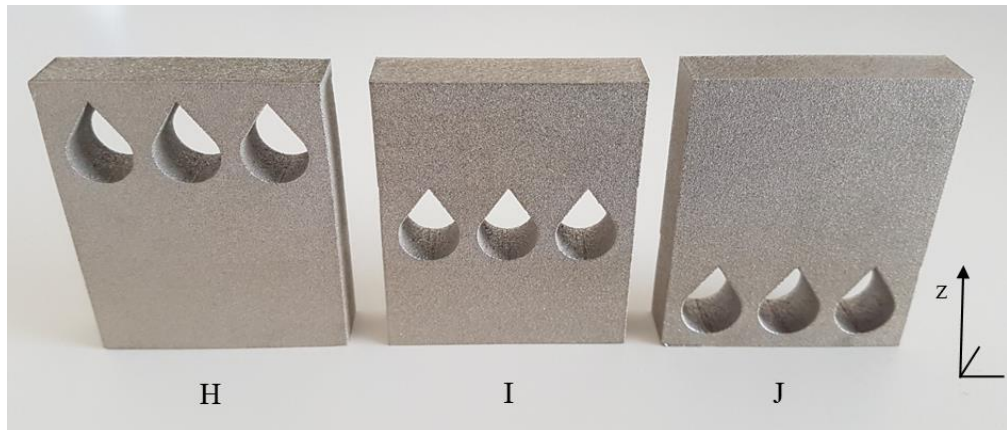
Figure 55. Test samples H, I and J. Building direction along z-axis.

No evident deformation can be observed in test samples represented in figure 55.

Macrographs of test samples H, I and J are shown in figure 56.
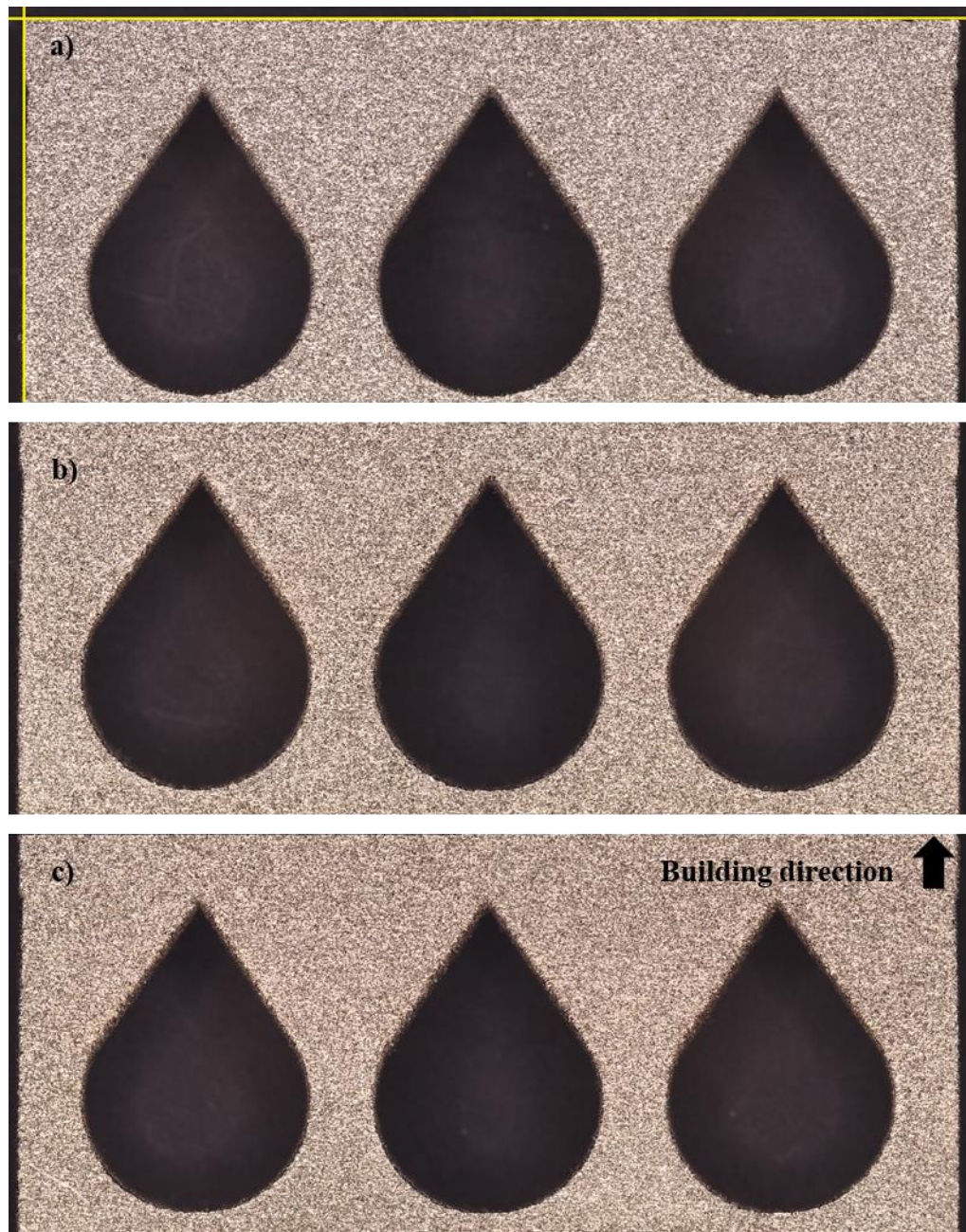
Figure 56. Macrographs of test samples (a) H, (b) I and (c) J. Front view, building direction is indicated with arrow.

The region of the holes in test samples H, I and J (see figure 56) was captured as thin walls between the holes may accumulate heat which may result in distortion. The holes are at different height of the part in each test sample, as it can be seen in figure 55. In test sample H the holes are in the top of the part and in test sample J the holes are at the bottom of the part (see figure 55). Therefore, the heat transfers through the thin walls of test sample J during almost the whole build (see in figure 39) whereas in test sample H, the heat transfers

through the thin walls only at the end of the build because they are built not until the end of the build. However, no deformation can be seen in the macrographs which indicates that there was not excessive accumulation of heat in any of the test samples to cause deformation, despite the location of the holes. None of the vertically built test samples had deformation in the experiments.

Based on the experiments executed in this thesis, horizontally built parts are more vulnerable to have deformations compared to parts built vertically (see for example figure 52). Especially the parts that were built horizontally flat were the ones to have deformation in the experiments whereas the parts that were built horizontally on their sides, did not have deformation. The test samples built horizontally on their sides are higher in the building direction and they have more stiffness in the building direction to resist the deformation, as demonstrated in figure 46. No evident deformations could be observed in most of the test samples manufactured. In fact, test samples C2, C4 and G2 (see figures 45b, 45d and 52b) were the only ones of all test samples to show evident deformation. The deformation shape of test samples C2, C4 and G2 obey the TGM and cool-down mechanism which pursue to bend the edges of the parts upwards from the building platform (Kruth et al. 2004, p. 617-618; Simson et al. 2017, p. 185). This behavior is observed also in the studies of Li et al. (2015, p. 709), Li et al. (2017, p. 167), Wu et al. (2014, p. 6264) and Yang et al. (2017, p. 612-614).

Each geometry was manufactured without deformation depending on the orientation of the test sample. It is obvious that deformation can be avoided by choosing correct building direction by adjusting part orientation. But it has to be noticed carefully when choosing suitable fabrication direction that the parts have different mechanical properties depending on the orientation they are built due to the layerwise manufacturing (Wohlers et al. 2018, p. 188-189). Tensile strength properties and surface roughness values are affected by the orientation of the part. Horizontally built parts have higher tensile strength compared to vertically built parts and sloped surfaces suffer from rough surface due to stair-step effect. (EOS 2018, p. 3-4.) Also building time and the need and location of support structures are affected by the orientation of part. Vertical building orientation requires more recoating time due to higher amount of layers (Wohlers et al. 2018, p. 198, 200).

Support structures are needed to support the overhanging features of the part and to fix the part to the building platform. Therefore, by changing the orientation of the part, it is possible to affect the need of support structures. It is also important to notice that the surfaces where support structures are attached, have rougher surface compared to surfaces without support structures. (Wohlers et al. 2018, p. 190-191.) Also capacity of the build can be affected by choosing orientation to allow building as many parts as possible in one build.

Deformation of metal parts is a common problem in L-PBF due to the cyclic heat delivery and residual stresses that are unavoidable in the process (Wohlers et al. 2018, p. 212). However, there are some ways to reduce the causes of cyclic heat delivery, such as by preheating the building platform which enables lower thermal gradients to occur due to lower temperature differences within the part (Mercelis & Kruth 2006, p. 264; Metal Additive Manufacturing 2018, p. 55). Also support structures have an impact on the resistance for deformations. Higher amount of support structures have more volume to transfer heat away from the part and fix the part more strongly to the building platform, in order to avoid warping. (Liu et al. 2016, p. 654; Wohlers et al. 2018, p. 210.) However, support structures are removed from the part after build which limits the usage of them as they can be challenging and costly to remove (Wohlers et al. 2018, p. 190, 210). Residual stresses of parts can also be reduced by thermal stress relief that can be performed after build once the loose powder has been removed from the parts. When thermal stress relief is performed, the parts are still attached to the building platform. In thermal stress relief the parts and the building platform are slowly heated up and held in high temperature for several hours, allowing the metal to go through metallurgical structural change. After that the parts are let cool down slowly in order to avoid tensions created by quick temperature change. (Wohlers et al. 2018, p. 212.)

The effect of heat is an important aspect that should be recognized when manufacturing parts with L-PBF. Parts can be ultimately complex by shape which creates challenges in the manufacturing as the heat transfers through the whole part towards the building platform and heat may locally accumulate strongly, inducing stresses to the part. Large areas require more scanning with laser which induces more heat to the part. The more heat is input in the part during the build, the more it will gain residual stress and expose for deformations (Mercelis & Kruth 2006, p. 256-257).

7 CONCLUSIONS

L-PBF is a promising manufacturing method for producing unique, high-performance end-use metal parts as it allows to produce such geometries that cannot be made with other manufacturing technologies. However, L-PBF has its limitations due to the cyclic heat delivery that causes residual stresses in parts and the stresses can rise on a level that causes deformations in the parts, which may make them unusable in their function.

Aim of this thesis was to recognize the deformation behavior of metal parts manufactured by L-PBF. The key was to clarify why deformations occur in metal parts made by L-PBF and what is the deformation shape. This thesis was done as literature review which is theoretical frame to the thermal phenomena and their effect on the formation of deformations in L-PBF of metal, and experimental part which is a practical part of this thesis to study the deformation behavior of stainless steel parts in L-PBF. Purpose of this thesis was to find and explain the causes behind the deformations of metal parts in L-PBF.

In L-PBF, a single hatch experiences multiple thermal cycles during the build as a hatch may melt and solidify several times but also conducts heat in the build. Hatch melts when exposed to laser beam but re-melts and solidifies again due to scanning of nearby hatches, depending on the geometry of the part and parameters of the build. These subsequent heating and cooling cycles induce residual stresses in the parts and expose the parts for deformations. (Li et al. 2017, p. 163-164; Mukherjee et al. 2018b, p. 372.)

Solid metal has higher thermal conductivity than powder metal which affects the heat transfer direction in the part during the build. In circumstances to have powder and solid material around the melt pool, the heat transfer direction is towards the solid material that includes the building platform and already solidified material. Circumstances that offer lower thermal conductivity around the melt pool result in larger melt pool and lower cooling rate and higher temperatures of the build. (Ilin et al. 2014, p. 399; Mukherjee et al. 2018b, p. 373-374.) When more layers are built, the heat will accumulate in the part and increase the part temperature which also leads to larger melt pool and reduced cooling rate of the melt pool (Ilin et al. 2014, p. 396; Mukherjee et al. 2018b, p. 374, 376-377). Based on these

aspects, it can be concluded that higher temperature causes larger melt pool and lower cooling rate. Higher temperature of the part lowers the yield strength of the material which increases its vulnerability to have deformations (Kruth et al. 2004, p. 617). In addition, the more heat is input to the part, the more residual stress it will gain (Mercelis & Kruth 2006, p. 256-257).

Tensile residual stresses are generated on the surface of the part whereas compressive stresses locate inside the part, which obeys the TGM and cool-down mechanism (Liu et al. 2016, p. 650-651; Mercelis & Kruth 2006, p. 256-257; Yang et al. 2017, p. 611, 613). Compressive stress reaches inside the building platform in addition to the part itself, exposing the upper section of the building platform under compressive stress and the lower section of the building platform under tensile stress (Mercelis & Kruth 2006, p. 257). Residual stresses induced by TGM pursue to bend the edges of parts upwards from the building platform (Kruth et al. 2004, p. 617; Simson et al. 2017, p. 185). Especially the parts that are orientated horizontally flat on the building platform are vulnerable to have deformation as seen in figures 22 and 23 (Wu et al. 2014, p. 6264). The TGM induces residual stresses despite the orientation of the part. Also vertically built parts are exposed to deformations as seen in figures 24 and 25 but the deformation appears larger in parts built horizontally. Residual stresses aim to lift the edges parts from the building platform and therefore the deformation shape depends on the orientation of the part on the building platform. For comparison, see figures 23 and 25 in which the same part is built horizontally flat and vertically. (Wu et al. 2014, p. 6264.)

Despite the scanning strategy, the highest residual stress peaks occur in the building direction rather than in horizontal plane because higher temperature gradients exist in the building direction (Li et al. 2017, p. 165; Liu et al. 2016, p. 651-652). Also the largest deformations occur along the building direction rather than horizontally (Wu et al. 2014, p. 6264). When it comes to horizontal plane, larger deformation occurs along the longer side of the part (Li et al. 2015, p. 709-710; Wu et al. 2014, p. 6264). Longer scanning vector causes higher stress value compared to shorter scanning vector (Liu et al. 2016, p. 653; Mercelis & Kruth 2006, p. 264). This occurs because longer tracks contract more than shorter ones and when the contraction is limited due to surrounding solid material, it results in higher residual stress in the longer tracks (Liu et al. 2016, p. 653).

Aim of the experimental part was to observe the deformation shape by studying different geometries positioned differently on the building platform. Purpose of the experimental part was to show the vulnerability of metal parts to have deformation in L-PBF but also to share ways to prevent the problem.

Test samples were made of EOS StainlessSteel 316L in a single run by L-PBF technology for metal materials, more specifically with EOS M 290 L-PBF machine. The test samples were analyzed with Keyence VR-3200 macroscope by capturing the surface of parts in a way that possible deformation of parts in the building direction, was observed.

Two sets of test samples were manufactured in the experiments of this thesis. In test set 1, rectangular shapes were built in different orientations (see table 9). Test samples C2 and C4 (represented in figures 45b and 45d) were the only ones of them to have deformation and they were both built in flat position. In test set 2 more varying geometries were built in different orientations (see table 10). The accumulation of heat along the building direction was pursued in test set 2 but as a result, none of the vertically built test samples had deformation and they all were manufactured successfully. The only test sample of test set 2 to have deformation was test sample G2 (see figures 51 and 52b), which was the one built horizontally flat.

All the test samples that were built vertically in the experiments, were successfully manufactured which tells that there was not excessive accumulation of heat and the heat was transferred through the test samples without causing problems. Also, the vertically built parts had features thick enough not to suffer from deformations due to the residual stresses. Based on the experiments, it can be stated that the orientation of the part plays an important role when it comes to the deformations of the part.

In addition to test samples C2 and G2, test samples B2, C1 and D1 (represented in figures 41, 43 and 48) were built in horizontal orientation but without deformation. Residual stresses induced by TGM pursue to lift the edges of parts from the building platform because tensile residual stress is generated on the top surface of parts in L-PBF (Kruth et al. 2004, p. 617; Simson et al. 2017, p. 185). Test samples C1 and D1 have more material in the building direction to resist the deformation compared to test samples C2 and G2. The same result

could be observed between test samples C4 and C5 (see in figures 45d and 45e) which were built in 45˚ angle. Then again, test sample B2 (20 mm) is remarkably shorter than test sample C2 (60 mm) or G2 (65 mm). Because smaller area contracts less, it makes it more difficult to capture the deformation in the smaller part (Liu et al. 2016, p. 653). The deformations observed in the experiments obey the TGM and cool-down mechanism, which complies with literature findings.

8   FURTHER STUDIES

Three of the test samples, C2, C4 and G2, had evident deformation in the experimental part of this thesis and based on the results, these test samples could be further researched. Aim of the further study would be to succeed in the build of these test samples without deformation, while being built in the same orientation as in this thesis. The geometries were built without deformation in vertical orientation in this thesis but the orientation of the part affects its mechanical properties which may prevent the utilization of different orientation. To succeed in the build without deformation, the effect of following ways to prevent the deformations, could be examined:

- Pre-heating of the building platform in several different temperatures
- Performing thermal stress relief
- Utilizing topology optimization in the design
- Utilizing simulation software to predict the deformation.

LIST OF REFERENCES

Bertoli, U.S., Guss, G., Wu, S., Matthews, M.J. & Schoenung, J.M. 2017. In-situ characterization of laser-powder interaction and cooling rates through high-speed imaging of powder bed fusion additive manufacturing. In: Materials and Design, 135. Pp. 385-396.

EOS. 2017. Material data sheet. EOS StainlessSteel 316L. [web document]. Pp. 4. Available: https://cdn0.scrvt.com/eos/7d9518b6b150de07/2e8cde1098a2/SS-316L_M290_Material_data_sheet_FlexLine_40_12-16_en.pdf.

EOS. 2018. Material data sheet. EOS StainlessSteel 316L. [web document]. Pp. 5. Available: https://cdn0.scrvt.com/eos/684f070e2e5e6323/47ee6cb0d51a/EOS_SS_316L_9011-0032_M400-4_Material_data_sheet_06-18_en.pdf.

EOS. 2019. EOS M 290. Available: https://cdn.eos.info/public/50bdb878a7784b60/c613d9d02d45daaf561fab22092bb827/EOS_M_290_left_download.jpg.

Ilin, A., Logvinov, R., Kulikov, A., Prihodovsky, A., Xu, H., Ploshikhin, V., Günther, B. & Bechmann, F. 2014. Computer aided optimization of the thermal management during laser beam melting process. In: Physics Procedia, 56. Pp. 390-399.

Kruth, J.P., Froyen, L., Van Vaerenbergh, J., Mercelis, P., Rombouts, M. & Lauwers, B. 2004. Selective laser melting of iron-based powder. In: Journal of Materials Processing Technology, 149. Pp. 616-622.

Le Roux, S., Salem, M. & Hor, A. 2018. Improvement of the bridge curvature method to assess residual stresses in selective laser melting. In: Additive Manufacturing, 22. Pp. 320-329.

Li, C., Fu, C.H., Guo, Y.B. & Fang, F.Z. 2015. A multiscale modeling approach for fast prediction of part distortion in selective laser melting. In: Journal of Materials Processing Technology, 229. Pp. 703-712.

Li, C., Liu, J.F., Fang, X.Y., & Guo, Y.B. 2017. Efficient predictive model of part distortion and residual stress in selective laser melting. In: Additive Manufacturing, 17. Pp. 157-168.

Li, Y. & Gu, D. 2014. Thermal behavior during selective laser melting of commercially pure titanium powder: Numerical simulation and experimental study. In: Additive Manufacturing, 1-4. Pp. 99-109.

Li, Y. Zhou, K., Tan, P., Tor, S.B., Chua, C.K. & Leong, K.F. 2018. Modeling temperature and residual stress fields in selective laser melting. In: International Journal of Mechanical Sciences, 136. Pp. 24-35.

Liu, Y., Yang, Y. & Wang, D. 2016. A study on the residual stress during selective laser melting of metallic powder. In: International Journal of Advanced Manufacturing Technology, 87. Pp. 647-656.

Masoomi, M., Thompson, S.M. & Shamsaei, N. 2017. Laser powder bed fusion of Ti-6Al-4V parts: Thermal modeling and mechanical implications. In: International Journal of Machine Tools & Manufacture, 118-119. Pp. 73-90.

Mercelis, P. & Kruth, J.P. 2006. Residual stresses in selective laser sintering and selective laser melting. In: Rapid Prototyping Journal, 12:5. Pp. 254-265.

Metal Additive Manufacturing. 2018. Fraunhofer ILT showcases VCSEL pre-heating for additive manufacturing. Metal Additive Manufacturing, 4:4. Pp. 55.

Mukherjee, T., Wei, H.L., De, A. & DebRoy, T. 2018a. Heat and fluid flow in additive manufacturing – Part I: Modeling of powder bed fusion. In: Computational Materials Science, 150. Pp. 304-313.

Mukherjee, T., Wei, H.L., De, A. & DebRoy, T. 2018b. Heat and fluid flow in additive manufacturing – Part II: Powder bed fusion of stainless steel, and titanium, nickel and aluminum base alloys. In: Computational Materials Science, 150. Pp. 369-380.

Renishaw. 2017. Design for metal AM. [web document]. Available: https://www.renishaw.com/en/design-for-metal-am-a-beginners-guide--42652.

Simson, T., Emmel, A., Dwars, A. & Böhm, J. 2017. Residual stress measurements on AISI 316L samples manufactured by selective laser melting. In: Additive Manufacturing, 17. Pp. 183-189.

Wohlers, T., Campbell, I., Diegel, O., Kowen, J., Fidan, I. & Bourell, D.L. 2018. Wohlers report 2018. 3D printing and additive manufacturing state of the industry annual worldwide progress report. Pp. 342.

Wu, A.S., Brown, D.W., Kumar, M., Gallegos, G.F. & King, W.E. 2014. An experimental investigation into additive manufacturing-induced residual stresses in 316L stainless steel. In: Metallurgical and Materials Transactions A, 45A. Pp. 6260-6270.

Yang, J. & Wang, F. 2008. 3D finite element temperature field modelling for direct laser fabrication. In: The International Journal of Advanced Manufacturing Technology, 43. Pp. 1060-1068.

Yang, Y.P., Jamshidinia, M., Boulware, P. & Kelly, S.M. 2017. Prediction of microstructure, residual stress, and deformation in laser powder bed fusion process. In: Computational mechanics, 61. Pp. 599-615.